


ARTICLE

# DNA damage promotes microtubule dynamics through a DNA-PK-AKT axis for enhanced repair

Shuyun Ma<sup>1,2</sup>, Zeming Rong<sup>1,2</sup>, Chen Liu<sup>1,2</sup>, Xiaobing Qin<sup>1,2</sup>, Xiaoyan Zhang<sup>3,4</sup>, and Qiang Chen<sup>1,2</sup> 

**DNA double-strand breaks (DSBs) are mainly repaired by c-NHEJ and HR pathways. The enhanced DSB mobility after DNA damage is critical for efficient DSB repair. Although microtubule dynamics have been shown to regulate DSB mobility, the reverse effect of DSBs to microtubule dynamics remains elusive. Here, we uncovered a novel DSB-induced microtubule dynamics stress response (DMSR), which promotes DSB mobility and facilitates c-NHEJ repair. DMSR is accompanied by interphase centrosome maturation, which occurs in a DNA-PK-AKT-dependent manner. Depletion of PCM proteins attenuates DMSR and the mobility of DSBs, resulting in delayed c-NHEJ. Remarkably, DMSR occurs only in G1 or G0 cells and lasts around 6 h. Both inhibition of DNA-PK and depletion of 53BP1 abolish DMSR. Taken together, our study reveals a positive DNA repair mechanism in G1 or G0 cells in which DSBs actively promote microtubule dynamics and facilitate the c-NHEJ process.**

## Introduction

DNA double-strand breaks (DSBs) greatly threaten the integrity of eukaryotic genomes, and incorrectly repaired DSBs lead to chromosomal aberrations and genome instability. To counteract the deleterious effects of DSBs, two major DSB repair pathways exist, canonical nonhomologous end joining (c-NHEJ) and homologous recombination (HR; Jackson and Bartek, 2009; Lukas and Lukas, 2013). HR operates relatively slower and is restricted to the S and G2 phases during the cell cycle, when sister chromatids are available as repair templates. In contrast to HR, c-NHEJ is a relatively fast and efficient process and functions throughout the cell cycle. In G1, DSBs are mainly repaired by c-NHEJ. Key components in c-NHEJ are the Ku70/Ku80 heterodimer, which could form a complex at DNA breaks with the DNA-dependent protein kinase catalytic subunit (DNA-PKcs), generating the DNA-PK holoenzyme (Jette and Lees-Miller, 2015). In G1 phase, c-NHEJ shows biphasic kinetics involving a fast and a slow process in response to ionizing radiation (IR)-induced DSBs (Biehs et al., 2017; Löbrich and Jeggo, 2017). The DNA ligase 4 complex, including XRCC4, XLF, and PAXX, carries out the direct ligation step of the two broken DNA ends in the later stages of c-NHEJ (Biehs et al., 2017; Ochi et al., 2015). The nuclease Artemis does not involve the fast end joining but is required for the slow end resection-dependent process (Biehs et al., 2017; Riballo et al., 2004). Mre11 exonuclease, EXD2, and Exo1 are also required for this end resection-dependent slow

NHEJ in G1 (Riballo et al., 2004). The slow NHEJ may contribute to the genomic instability in G1 (Biehs et al., 2017; Löbrich and Jeggo, 2017).

As DSBs are the most deleterious form of DNA damages, c-NHEJ and HR are highly regulated to avoid ectopic repair. End resection is required for HR in S or G2 cells, while the inappropriate resection in G1 impedes the initiation of the NHEJ repair process. 53BP1 is a crucial factor for c-NHEJ and limits the 5' resection of the broken ends in a cell cycle-dependent manner. 53BP1-bound Rif1 and Rev7-shieldin complex executes the inhibition of 5' end resection in G1 (Dev et al., 2018; Ghezraoui et al., 2018; Gupta et al., 2018; Mirman et al., 2018; Noordermeer et al., 2018; Xu et al., 2015). Interestingly, recent findings suggest that DSB-induced phosphorylation of CtIP by Plk3 in G1 could mediate CtIP-BRCA1 interaction, which regulates end resection-dependent slow c-NHEJ (Barton et al., 2014; Biehs et al., 2017; Löbrich and Jeggo, 2017). As both fast NHEJ and slow NHEJ contribute to the DSB repair in G1 cells, most DSBs should be repaired by fast NHEJ to avoid slow NHEJ-induced genomic instability. The underlying mechanism that regulates the choice between fast and slow NHEJ in G1 or G0 cells is still not clear.

DNA damage increases chromatin mobility, both locally at DSBs and genome wide (Hauer and Gasser, 2017). DSB mobility is regulated by several factors, including 53BP1, LINC (linker of

<sup>1</sup>Department of Radiation and Medical Oncology, Medical Research Institute, Zhongnan Hospital of Wuhan University, Wuhan University, Wuhan, China; <sup>2</sup>Frontier Science Center for Immunology and Metabolism, Medical Research Institute, Wuhan University, Wuhan, China; <sup>3</sup>College of Biomedicine and Health, Huazhong Agricultural University, Wuhan, China; <sup>4</sup>College of Life Science and Technology, Huazhong Agricultural University, Wuhan, China.

Correspondence to Qiang Chen: [C52616@hotmail.com](mailto:C52616@hotmail.com).

© 2020 Ma et al. This article is distributed under the terms of an Attribution-Noncommercial-Share Alike-No Mirror Sites license for the first six months after the publication date (see <http://www.rupress.org/terms/>). After six months it is available under a Creative Commons License (Attribution-Noncommercial-Share Alike 4.0 International license, as described at <https://creativecommons.org/licenses/by-nc-sa/4.0/>).

nucleoskeleton and cytoskeleton) complex, microtubule, nuclear actin, Lamin A/C, and IFFO1 (Caridi et al., 2018; Lawrimore et al., 2017; Li et al., 2019; Lottersberger et al., 2015; Schrank et al., 2018). For instance, the increase of DSB mobility requires 53BP1 and dynamic microtubules, which act through the LINC complex and kinesins on the nuclear envelope (Lawrimore et al., 2017; Lottersberger et al., 2015). In G1, mobile DSBs could increase their exploration and promote end joining (Lottersberger et al., 2015). However, mobility of DSBs should be tightly regulated, as increased mobility of DSBs can also be a source of genomic translocation (Li et al., 2019; Roukos et al., 2013). As microtubule dynamics are one of the factors for DSB mobility (Lottersberger et al., 2015), the regulation of microtubule dynamics is crucial for DSB mobility and repair. Thus, we set out to study whether the microtubule dynamics will change after DNA damage and, if so, what is the underlying mechanism.

The centrosome is the major microtubule organizing center and comprises of a pair of centrioles and the surrounding pericentriolar material (PCM), which contains the key microtubule nucleation molecules, including  $\gamma$ -tubulin ring complex (Moritz et al., 2000; Zheng et al., 1995), NEDD1, and pericentrin (PCNT; Woodruff et al., 2014; Zhang et al., 2009). The centrosome undergoes a maturation process as cells progress toward mitosis, in which PCM increases in size and promotes its microtubule nucleation capacity (Palazzo et al., 2000). The communication between the centrosome and DNA damage response (DDR) has been reported in different conditions (Mullee and Morrison, 2016). Several DDR proteins, such as ATM, ATR, DNA-PKcs, CHK1 and CHK2 kinases, and the BRCA1 ubiquitin ligase complex, have been found at the centrosomes (Mullee and Morrison, 2016). Some centrosome proteins, such as centrin2 and PCNT, have been shown to stimulate DDR and are required for efficient nucleotide excision repair (Griffith et al., 2008; Mullee and Morrison, 2016; Nishi et al., 2005). DNA-damaging treatment causes significant alterations in centrosome structures and promotes centrosome duplication, leading to multicentrosomal cells (Bourke et al., 2007; Dodson et al., 2007; Löffler et al., 2013). Although the relationship between DNA damage and the centrosome has been widely studied, the short-term effect of DSBs on the centrosome and microtubule dynamics is still a mystery, as most of the studies focused on the long-term effect (>12 h) on the centrosome after DNA-damaging treatment. Considering the fast NHEJ process only lasts around 4 h (Löbrich and Jeggo, 2017), we examined the short-term effect of DSBs on the centrosome and microtubule dynamics.

In this study, we found that DSBs promoted microtubule dynamics in G1 or G0 phase cells. We named this specific microtubule response as DSB-induced microtubule dynamics stress response (DMSR). Alteration of DMSR affects the c-NHEJ process and leads to genomic instability.

## Results

### DSBs promote microtubule polymerization in G1 phase cells

To study the effect of DNA damage on the microtubule network, we first synchronized U2OS cells in G1 phase by a double thymidine treatment in which cells have relatively low microtubule

dynamics. Synchronized cells were treated with 2 Gy IR and released for the indicated time points (Fig. S1 A). The centrosome-dependent microtubule polymerization rate was determined by microtubule length in a microtubule regrowth assay. Intriguingly, the rate of microtubule polymerization started to rise at 2 h and peaked at 4 h after IR. This effect gradually diminished at 6 h after IR (Fig. 1, A and B). The same effect of DSBs on microtubules was also observed in MCF7 (Fig. 1, C and D), HeLa cells (Fig. 1 E), and nontransformed RPE-1 (retinal pigment epithelium) cells (Fig. 1 F), indicating that the observations were a general response of microtubule dynamics to DNA damage. The DDR activation and DNA damage repair kinetics were determined by 53BP1 or  $\gamma$ H2AX foci formation (Fig. 1 G), which represented DSB sites in the nucleus. We hypothesized that the increased microtubule polymerization rate was caused by IR-induced DSBs. To test our hypothesis, we treated cells with bleomycin, which is a radiomimetic agent that causes DSBs directly (Robles and Adami, 1998). The same effect was observed in G1 cells treated with bleomycin (Fig. 1 H). On the contrary, UV treatment, which does not directly lead to DSBs (Rastogi et al., 2010), did not affect the microtubule nucleation in G1 cells. These results suggested that the DNA damage-induced promotion of microtubule polymerization was DSB specific. As the centrosome in G1 phase cells normally has low microtubule nucleation activity and the effect lasts only around 4–6 h after DNA damage treatment (Fig. 1, B and F), we speculate that this effect was a DMSR accompanied by a short-term increase of centrosome-dependent microtubule polymerization. To examine whether DMSR was a stress response, we treated G1 phase cells with different doses of IR and found that, although DMSR could be observed when cells were treated with 1 Gy IR, the extent of DMSR rose significantly when we elevated the dose of IR treatment (Fig. 1 I). The same effect was also found in MCF7 cells (Fig. 1, C and D). These results implied that DMSR is a DSB dose-dependent stress response in the microtubule network, which lasts around 4–6 h after DNA damage treatment and could be only induced by DSBs.

### DMSR promotes both the centrosome-dependent microtubule polymerization and microtubule nucleation

Most microtubules originate from the centrosome, and microtubule regrowth assay is normally used to determine the extension rate of microtubule polymerization from the centrosome. As the rate of microtubule polymerization is distinct from centrosome-dependent microtubule nucleation capacity, we studied the relationship between DMSR and these two aspects of microtubule dynamics. From the inverted grayscale images of microtubule regrowth assay (Fig. S1, B and C), we observed that IR treatment clearly led to an increased number of microtubules that originated from the centrosome, although the exact number of microtubules in each time point is hard to quantitate. Due to the difficulty in quantifying the microtubule numbers in microtubule regrowth assay, we employed RPE-1 cells exogenously expressing GFP-tagged EB3 (end-binding protein 3) to check microtubule dynamics. GFP-EB3 served as a marker for the plus-end tips of each growing microtubule (Komarova et al., 2005). Thus, the mobility of the GFP-EB3

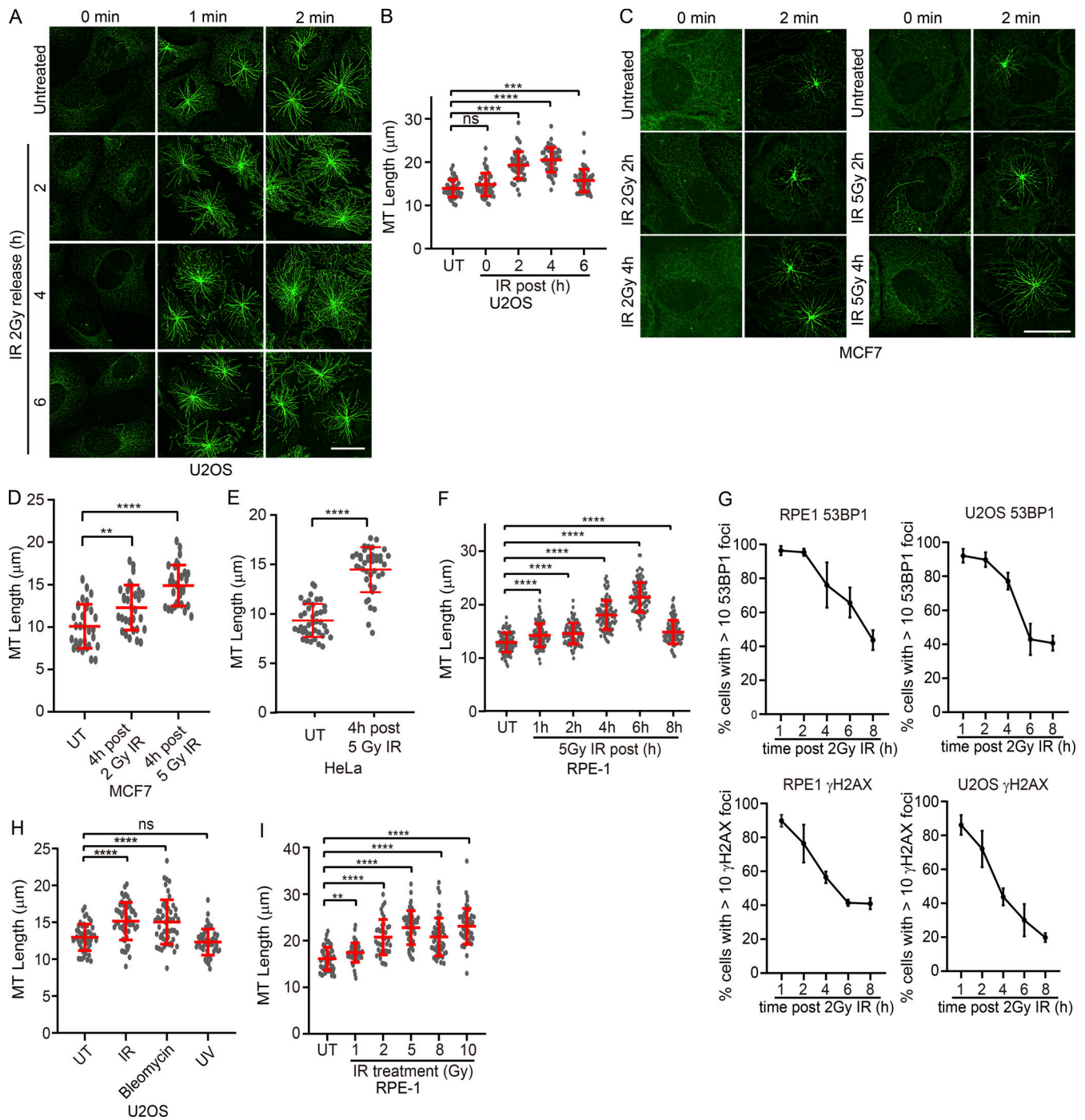
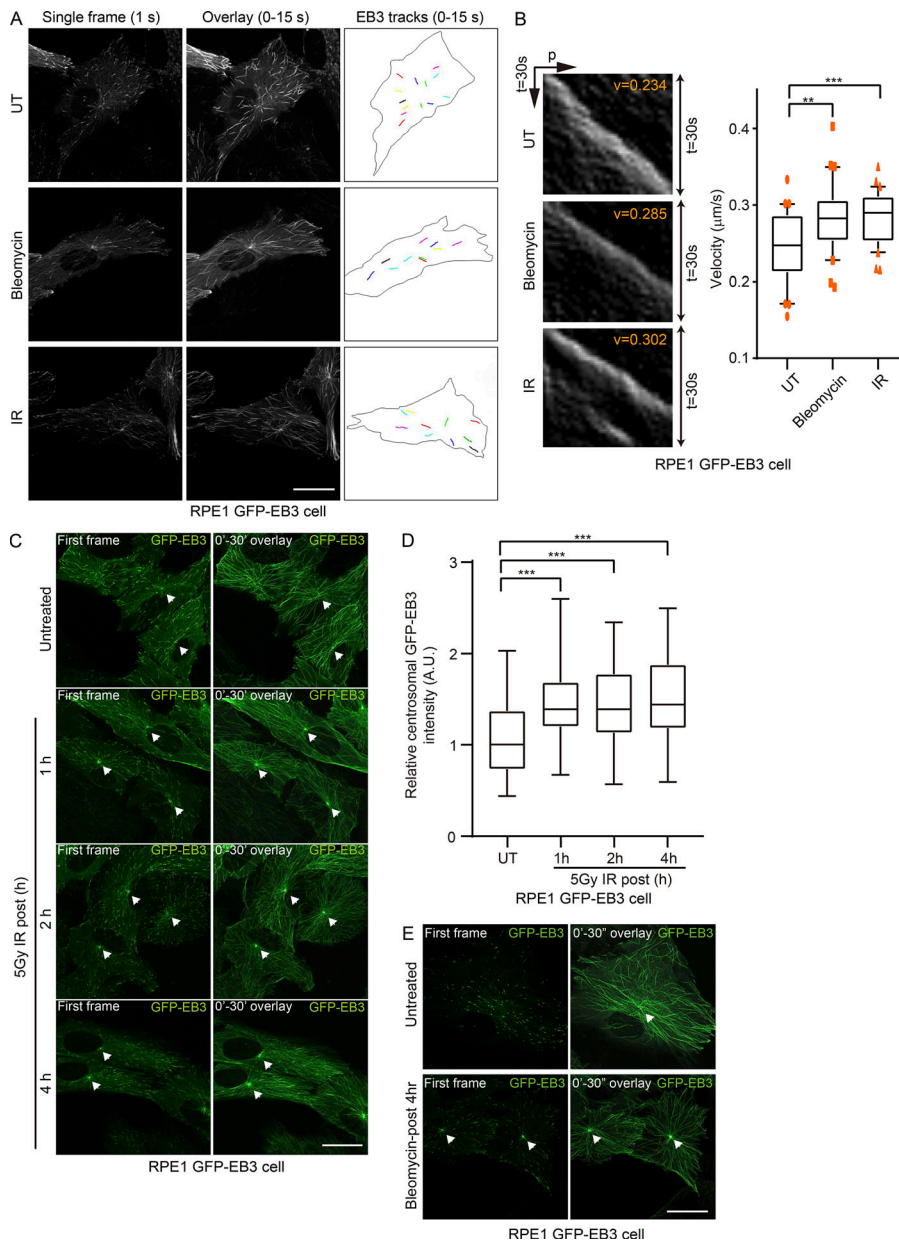


Figure 1. **DSBs promote microtubule dynamics in G1 cells.** (A) U2OS at G1/S phase were treated with 2 Gy IR, released, and fixed at indicated time points. Microtubules (green) were stained with anti- $\beta$ -tubulin antibody in microtubule regrowth assay. Scale bar, 20  $\mu\text{m}$ . (B) Quantitation of microtubule length after IR as assayed in A showed the rate of microtubule polymerization ( $n > 50$ ). (C) Microtubule regrowth assay was performed in G1 MCF7 cells 4 h after IR. Scale bar, 20  $\mu\text{m}$ . (D) Quantitation of microtubules length 4 h after treatment with different doses of IR in G1 MCF7 cells ( $n > 50$ ). (E) Quantitation of microtubule length 4 h after 5 Gy IR treatment in G1 HeLa cells. (F) Quantitation of microtubule length after IR in G1 RPE-1 cells ( $n > 50$ ). (G) The kinetics of DNA damage repair were determined by 53BP1 or  $\gamma\text{H2AX}$  foci formation ( $n > 100$ ). (H) Quantitation of microtubule length 4 h after indicated treatment in G1 U2OS cells ( $n > 50$ ). (I) Quantitation of microtubule length 4 h after treatment with indicated doses of IR in G1 RPE-1 cells ( $n > 50$ ). P values are from un-paired  $t$  test: \*\*\*\*,  $P < 0.0001$ ; \*\*\*,  $P < 0.001$ ; \*\*,  $P < 0.01$ ; \*,  $P < 0.05$ ; ns, not significant. Values are shown as mean  $\pm$  SD in this and following experiments. MT, microtubule; UT, untreated.



**Figure 2. Both microtubule polymerization and microtubule nucleation were promoted during DMSR.** (A) GFP-EB3 comet tracks were recorded in RPE-1 cells under indicated treatments. Images of projections at 1 s (single frame), spanning 0–15 s (overlay), and representative EB3 comet tracks spanning 15 s with different colors are shown. Comets tracks were generated with KymographClear 2.0 and KymographDirect 2.1 in ImageJ software (see also Videos 1, 2, and 3). Scale bar, 20  $\mu\text{m}$ . (B) Left: Representative kymograph images for the measurement of EB3 comet velocity. Right: Box plot shows quantitative analysis of GFP-EB3 comet velocities in live G1 phase GFP-EB3-expressing RPE-1 cells under different treatments. Center line, median; box limits, 25th and 75th percentile; whiskers, fifth and 95th percentile (see also Materials and methods). (C) Centrosome-dependent microtubule nucleation capacity was determined by live-imaging time-lapse experiments in G1 RPE-1 cells. Left: The first single frame of GFP-EB3 in steady status was shown. Right: Overlaid images showed increased centrosomal GFP-EB3 signals after IR. Arrowheads indicate centrosomes where GFP-EB3 signal was started (see also Videos 4, 5, 6, and 7). Scale bar, 20  $\mu\text{m}$ . (D) Quantitative analysis of relative centrosomal GFP-EB3 intensity in overlaid images as in C was shown in box plot ( $n > 30$ ). (E) Live-imaging time-lapse experiments of GFP-EB3 were performed in G1 RPE-1 cells 4 h after bleomycin treatment. Arrowheads indicate centrosomes where GFP-EB3 signal was started (see also Videos 8 and 9). Scale bar, 20  $\mu\text{m}$ . \*\*\*,  $P < 0.001$ ; \*\*,  $P < 0.01$ . A.U., arbitrary units; UT, untreated.

signal indicates the extension rate of microtubule polymerization, while the intensity of GFP-EB3 signals that originated from the centrosome within a specific period could be used to measure the centrosome-dependent microtubule nucleation capacity.

Using RPE-1 cells expressing GFP-EB3, the effect of DMSR on the extension rate of microtubule polymerization was first confirmed by time-lapse fluorescent imaging experiment (Fig. 2, A and B; Fig. S1 D; and Videos 1, 2, and 3). Representative GFP-EB3 comet tracks are presented in different colors for each treatment, and, obviously, the comet tracks in bleomycin- or IR-treated cells are longer than the tracks in untreated cells (0–15 s; Fig. 2 A). The measurement of the velocity of EB3 comets further supported that the mobility of GFP-EB3 increased significantly in IR- or bleomycin-treated cells (Fig. 2 B), indicating DSBs lead to increased rates of microtubule polymerization.

As GFP-EB3 locates on the microtubule plus end, GFP-EB3 was used to track the newly nucleated microtubules and to determine the emanation rate from the centrosome (Colello et al., 2012). Thus, we analyzed the GFP-EB3 signals originating from the centrosome within 30 s through a live-imaging time-lapse experiment (Fig. 2 C; Videos 4, 5, 6, and 7). In total, 30 images were recorded for every 1 s and overlaid in one image. The centrosomal GFP-EB3 intensity in the overlaid image was used to indicate the number of newly nucleated microtubules that originated from the centrosome within 30 s (Fig. 2 C, right). Remarkably, IR treatment led to increased centrosomal intensity of GFP-EB3, which started from 1 h and, with continuous effect, lasted until 4 h after IR (Fig. 2, C and D), suggesting that IR treatment increased the centrosome-dependent microtubule nucleation capacity. Bleomycin treatment displayed the same enhanced intensity of centrosomal GFP-EB3 (Fig. 2 E; Videos 8

and 9). These data demonstrated that DMSR is accompanied with both increased a microtubule polymerization rate and enhanced microtubule nucleation capacity.

### DMSR only occurs in G0 or G1 cells

Next, we asked whether DMSR occurred in another cell cycle phase besides G1. First, we examined DMSR in G0 cells. U2OS cells were synchronized in G0 by serum starvation and then treated with bleomycin for 2 h. After release from bleomycin treatment for the indicated time points, DMSR was checked with the microtubule regrowth assay (Fig. S2 A). Quantitative analysis of microtubule length confirmed that DMSR also happened in G0 cells and that DMSR lasted for around 4–6 h after DNA damage (Fig. 3, A and B). The DNA damage repair kinetics after bleomycin treatment were determined by 53BP1 foci formation (Fig. 3 C). We observed the same microtubule dynamics in G0 cells after IR-induced DSBs (Fig. 3 D). To determine whether DMSR happened in S phase cells, U2OS cells were released from double thymidine block for 3 h or 5 h to allow cells to enter S phase. The procedure for this experiment was interpreted in Fig. S2 B, and the cell cycle stage was determined by flow cytometry. DMSR was then examined by microtubule regrowth assay 2 h after IR. From the flow cytometry data, we found that cells were still in G1 phase after being released from IR for 2 h (Fig. S2 B), and, accordingly, DMSR occurred as indicated by increased microtubule length (Fig. 3 E, lane 2). Intriguingly, the extent of DMSR significantly decreased in S phase cells when the cells were released from double thymidine block for 3 h, and DMSR totally disappeared when cells were released for 5 h from double thymidine block (Fig. 3 E).

As a complementary approach, we also analyzed DMSR in asynchronously dividing cells. DMSR was determined by microtubule regrowth assay at 1 h or 2 h after IR. To differentiate G1 from S/G2 cells, we coimmunostained  $\beta$ -tubulin with cyclin A in microtubule regrowth assay, which is restricted to S/G2 (Fig. 3 F; [Escribano-Díaz et al., 2013](#)). Quantitative analysis of microtubule length indicated that DMSR only happened in cyclin A-negative cells (Fig. 3 G). These results suggest that DMSR is restricted in G0 or G1 cells.

### NHEJ pathway is involved in the regulation of DMSR

As c-NHEJ is the predominant DSB repair pathway in G1 or G0 cells, we hypothesized that the c-NHEJ pathway may participate in DMSR. Consistent with our hypothesis, the DNA-PK inhibitor, but not ATM or ATR inhibitor treatment, abolished DMSR (Fig. 4 A and Fig. S3 A). We got the same result with DNA-PKcs depletion (Fig. 4 B). The Ku70/Ku80 heterodimer is required for DNA-PK activation and c-NHEJ initiation. DMSR disappeared after depletion of Ku70 or Ku80, which further confirmed the role of DNA-PK in DMSR (Fig. 4 B). As DNA-PKcs autophosphorylation on Ser2056 could be a marker for DNA-PK activation, we probed the whole U2OS cell extracts with an anti-pS2056 DNA-PKcs antibody and found that activation of DNA-PK was observed 2 h after IR and gradually decreased from 6 h (Fig. S3 B), which was consistent with the time course of DMSR. The efficiency of DNA-PKcs, Ku70, or Ku80 depletion was checked by Western blot or quantitative PCR (Fig. S3 C). All

these results indicate that DNA-PK activity is important for DMSR.

On the contrary, depletion of Artemis, another key factor in NHEJ, did not affect DMSR positively or negatively (Fig. 4 B). Previous reports showed that IR-induced DSBs are repaired by fast and slow c-NHEJ processes in G1 phase cells, and Artemis nuclease is specifically required for the slow but not fast NHEJ process ([Biehs et al., 2017](#); [Löbrich and Jeggo, 2017](#)). The slow c-NHEJ process in G1 phase cells is accompanied by end resection, which depends on CtIP, EXD2, EXO1, and NBS1 ([Biehs et al., 2017](#)). Depletion of these proteins did not have an effect on DMSR (Fig. S3 D), suggesting that end resection-dependent slow NHEJ was dispensable for DMSR.

DSBs could be repaired by c-NHEJ or HR, and the choice was tightly regulated, especially in G1 cells, since there is no DNA template required for HR repair in G1. 53BP1 and Shieldin complex promotes c-NHEJ and inhibits HR ([Dev et al., 2018](#); [Findlay et al., 2018](#); [Ghezraoui et al., 2018](#); [Gupta et al., 2018](#); [Mirman et al., 2018](#); [Noordermeer et al., 2018](#); [Tomida et al., 2018](#)). Thus, we examined the effect of 53BP1 and the Shieldin complex on DMSR and found that depletion of 53BP1 or Shieldin complex, such as with FAM35A, REV7/RINN2, or RINN1, could affect DMSR (Fig. 4 C; and Fig. S3, E and F), indicating that 53BP1 and Shieldin complex were involved in DMSR.

The complex of Ligase 4, XRCC4, and XLF is responsible for direct DSB ligation, which is the final step of c-NHEJ ([Pannunzio et al., 2018](#)). To further study the effect of c-NHEJ on DMSR, we knocked down Ligase 4, XRCC4, or XLF by siRNA to sustain the active c-NHEJ process and found that depletion of these proteins significantly enhanced the extent of DMSR compared with scrambled siRNA-treated cells (negative control [NC]; Fig. 4 D; and Fig. S3, G and H). Furthermore, DMSR could still be obviously observed at 8 h after IR in siLigase 4-treated cells (Fig. 4 E), indicating that DMSR was prolonged. Consistent with this result, DNA damage repair kinetics in Ligase 4-depleted cells were greatly delayed (Fig. S3 I), indicating that accumulation of DSBs in IR-treated Ligase 4-depleted cells may enhance DMSR. Meanwhile, we found that in XLF, XRCC4, or Ligase 4-depleted cells without IR treatment, microtubule dynamics were higher than in control U2OS cells (Fig. 4, D and E), indicating that accumulated DSBs caused by inactive ligation might continuously activate the NHEJ pathway and cause sustained DNA-PK activation, which further leads to increased microtubule dynamics. These results demonstrated that prolonged c-NHEJ caused by Ligase 4, XRCC4, or XLF depletion enhances and prolongs DMSR.

Using time-lapse fluorescent imaging experiments, the velocity of the GFP-EB3 track was also measured in cells treated with scrambled siRNA, siLigase 4, or si53BP1. The velocity of EB3 comets increased in cells treated with scrambled siRNA after IR. The extent of the increase of the DSB-induced velocity was further enhanced in cells treated with siLigase 4. On the contrary, we did not observe obvious DSB-induced changes in the velocity of GFP-EB3 in si53BP1-treated cells (Fig. 4 F). The centrosomal GFP-EB3 intensity was determined as in Fig. 2 C and was also increased in siLigase 4-treated cells but not in si53BP1-treated cells (Fig. 4 G), indicating that centrosome-dependent microtubule nucleation capacity was enhanced in siLigase 4

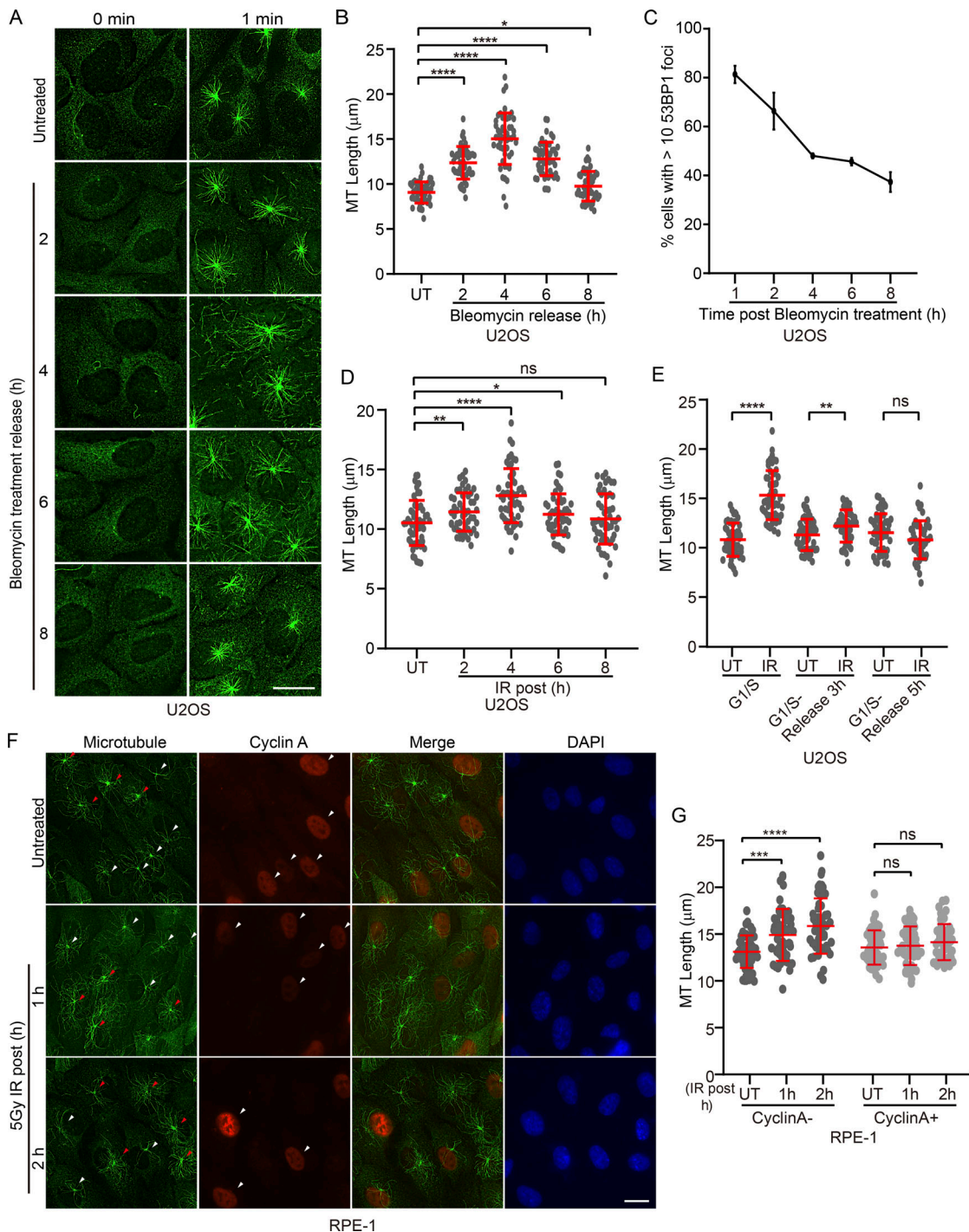
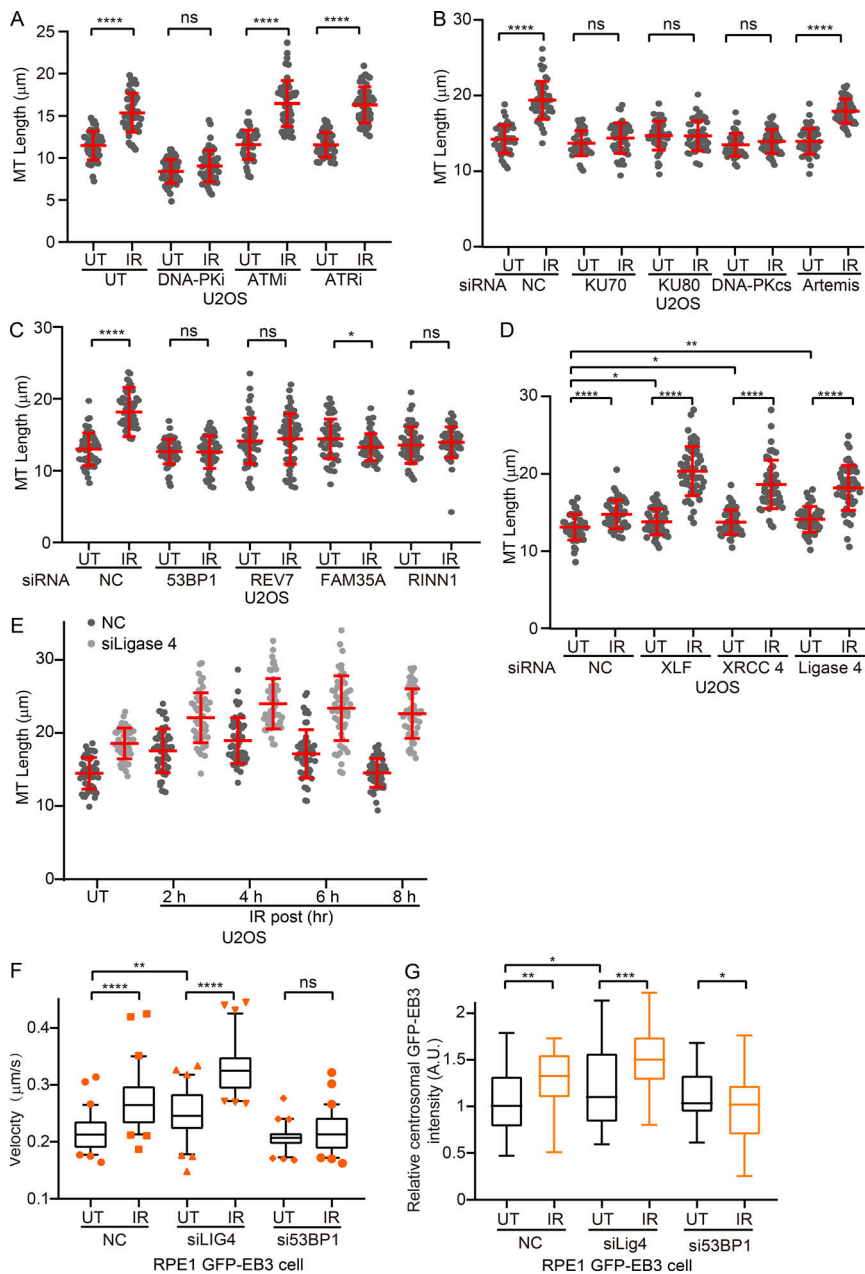


Figure 3. **DMSR only occurs in G0 or G1 cells.** (A) Microtubule regrowth assay was performed in G0 cells after bleomycin treatment. Microtubules (green) were stained with anti- $\beta$ -tubulin antibody. Scale bar, 20  $\mu\text{m}$ . (B) Quantitation of microtubule length after bleomycin treatment in G0 cells as in A was shown ( $n > 50$ ). (C) The kinetics of DNA damage repair in bleomycin-treated cells were determined by 53BP1 foci formation ( $n > 100$ ). (D) Quantitation of microtubule length in G0 cells after IR is shown ( $n > 50$ ). (E) DMSR happens in G1 but not in S phase. Quantitation of microtubule length is shown ( $n > 50$ ). The detailed procedure is shown in Fig. S2 B. (F) Microtubule regrowth assay was performed in asynchronous cells after IR. Cells were costained with anti- $\beta$ -tubulin (green) and anti-cyclin A (red) antibodies. White arrowheads indicate cyclin A-positive cells and red arrowheads indicate cyclin A-negative cells. Scale bar, 20  $\mu\text{m}$ . (G) Quantitation of microtubule length in cyclin A-negative and cyclin A-positive cells is shown ( $n > 50$ ). \*\*\*\*,  $P < 0.0001$ ; \*\*\*,  $P < 0.001$ ; \*\*,  $P < 0.01$ ; \*,  $P < 0.05$ ; ns, not significant. MT, microtubule; UT, untreated.



**Figure 4. c-NHEJ pathway is indispensable for DMSR.** (A) DMSR was examined when cells were treated with DNA-PK, ATM, or ATR inhibitors. Quantitation of microtubule length is shown ( $n > 50$ ). (B) DMSR was examined in cells with depletion of indicated genes. Quantitation of microtubule length is shown ( $n > 50$ ). Cells were transfected with an equal amount of scrambled siRNA as an NC. (C) 53BP1 regulated DMSR. DMSR was examined in cells with depletion of indicated genes. Quantitation of microtubule length is shown ( $n > 50$ ). (D) Depletion of Ligase 4, XRCC4, or XLF increases the extent of DMSR. Quantitation of microtubule length is shown ( $n > 50$ ). (E) Depletion of Ligase 4 prolongs the time course of DMSR. Quantitation of microtubule length is shown ( $n > 50$ ). (F) Box plot shows quantitative analysis of GFP-EB3 comet velocity in live siRNA-treated GFP-EB3-expressing G1 RPE-1 cells ( $n > 30$ ). (G) Centrosome-dependent microtubule nucleation capacity was determined by relative centrosomal GFP-EB3 intensity in live siRNA-treated GFP-EB3-expressing G1 RPE-1 cells, and quantitative analysis is shown in box plot ( $n > 30$ ). \*\*\*\*,  $P < 0.0001$ ; \*\*\*,  $P < 0.001$ ; \*\*,  $P < 0.01$ ; \*,  $P < 0.05$ ; ns, not significant. A.U., arbitrary units; MT, microtubule; UT, untreated.

but not in si53BP1 cells. All these results suggested that DMSR may be activated when fast NHEJ fails to repair DSBs.

**DMSR is accompanied by interphase centrosome maturation**

As the centrosome is the major microtubule organization center, we further investigated the effect of DSBs on the centrosome to explore the underlying mechanism of DMSR. We observed a dramatic accumulation of centrosome-associated proteins on the centrosome in G1 cells at 4 h after IR, including PCMs, such as PCNT,  $\gamma$ -tubulin, and NEDD1 (Fig. 5 A). Intriguingly, DMSR was abolished after NEDD1 or PCNT depletion (Fig. 5 B and Fig. S4 A). PCNT-depleted cells remained in G1 phase at 4 h post-IR as determined by flow cytometry (Fig. S4 B). These results indicate that DSBs induce DMSR through the accumulation of PCM proteins at the interphase centrosome.

The accumulation of PCM proteins on the centrosome is typically a hallmark of centrosome maturation during G2 phase and mitosis. The normal centrosome maturation process in G2 cells depends on Polo-like kinase 1 (PLK1) and results in an increased ability of the centrosome to nucleate microtubules (Barr et al., 2004). To examine whether DMSR is operated through the classical centrosome maturation mechanism, we inhibited PLK1 with a PLK1 inhibitor and found there were no detectable changes in DSB-induced PCM protein accumulation at the centrosome (Fig. 5 C and Fig. S4 C), and DMSR was also not affected (Fig. 5 D), suggesting that DSB-induced PCM recruitment at the interphase centrosome depends on different pathways.

Based on the fact that DSBs lead to accumulation of PCMs at the interphase centrosome and an elevated microtubule polymerizing rate in G1 or G0 cells, we uncovered a novel DSB-induced

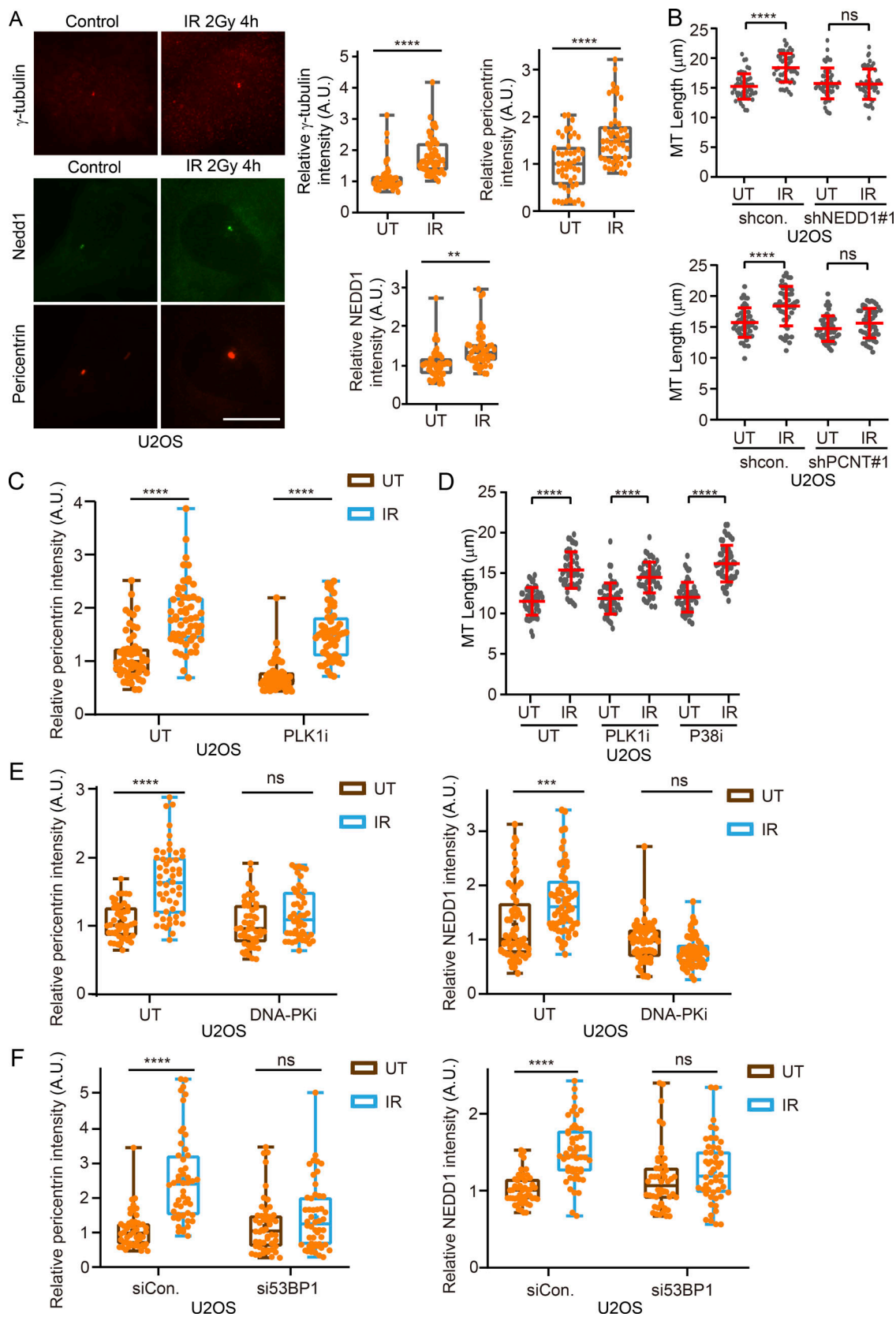


Figure 5. **DSBs induce accumulation of PCM proteins at the centrosome.** (A) Left: NEDD1, PCNT, and  $\gamma$ -tubulin were recruited to the centrosomes in G1 cells 4 h after IR. Right: Semiquantitative analysis of the relative immunostaining signal intensity of PCM proteins at the centrosomes in control or IR-treated U2OS cells was shown in box plot. Scale bar, 20  $\mu$ m. (B) DMSR was determined in G1 cells treated with scrambled shRNA, shNEDD1, or shPCNT1. Quantitation of microtubule length is shown ( $n > 50$ ). (C) Semiquantitative analysis of relative PCNT signal intensity at the centrosomes in control or PLK1 inhibitor-treated



G1 cells is shown in box plot ( $n > 50$ ). **(D)** G1 cells were pretreated with PLK1 or P38 inhibitor for 30 min and exposed to 2 Gy IR. DMSR was determined 4 h after IR. Quantitation of microtubule length in control, PLK1 inhibitor, or p38 inhibitor treated cells is shown ( $n > 50$ ). **(E)** Semiquantitative analysis of relative PCNT or NEDD1 signal intensity at the centrosomes from control or DNA-PK inhibitor-treated G1 cells is shown in box plot ( $n > 50$ ). **(F)** Semiquantitative analysis of relative PCNT or NEDD1 signal intensity at the centrosomes in G1 cells treated with scrambled (NC) siRNA or si53BP1 is shown in box plot ( $n > 50$ ). For box plot, center line, median; box limits, 25th and 75th percentile; whiskers, minimum and maximum (see also Materials and methods). \*\*\*\*,  $P < 0.0001$ ; \*\*\*,  $P < 0.001$ ; \*\*,  $P < 0.01$ ; ns, not significant. A.U., arbitrary units; MT, microtubule; UT, untreated.

interphase centrosome maturation process. Actually, this interphase centrosome maturation induced by DSBs is similar to bacterial lipopolysaccharide (LPS)-induced centrosome changes (Vertii et al., 2016). P38 and JNK MAPKs have been implicated in the interphase centrosome maturation in LPS-stimulated cells. To examine whether these two processes share a similar mechanism on interphase centrosome maturation, we chemically inhibited P38 and did not observe an obvious effect on DMSR (Fig. 5 D and Fig. S4 C), suggesting that DSB-induced interphase centrosome maturation may have a distinct mechanism from LPS-induced centrosome maturation.

As we found that DNA-PK and c-NHEJ are required for DMSR, we next examined the function of DNA-PK and c-NHEJ on PCM recruitment at the centrosome. Although DNA-PK has been reported as an important regulator of mitotic spindle formation (Shang et al., 2010), the role of DNA-PK on the interphase centrosome is still unknown. DNA-PK inhibitor (Fig. 5 E) and 53BP1 depletion (Fig. 5 F) affected PCM recruitment at the centrosome after IR, indicating that c-NHEJ may participate in DSB-induced interphase centrosome maturation. The major subdistal appendage proteins, Ninein and CEP170, which are crucial for microtubule anchoring, also dramatically accumulated at the interphase centrosome after IR (Fig. S4 D). DNA-PK inhibition or 53BP1 knockdown abolished the DSB-induced accumulation of Ninein and CEP170 (Fig. S4 E), indicating that DSBs induce comprehensive changes on the interphase centrosome through DNA-PK, which leads to DMSR.

#### DMSR requires centrosomal AKT activation

Next, we aimed to uncover the downstream factor of DNA-PK on DMSR. Protein kinases, such as CHK1, CHK2, and AKT, which regulate the centrosome structure or functions, have been reported as downstream factors of DNA-PK (Bozulich et al., 2008; Buttrick et al., 2008; Li and Stern, 2005; Lin et al., 2014; Löffler et al., 2007; Wang et al., 2015). CHK1 and CHK2 are key components of DNA damage-activated checkpoint signaling response (Bartek and Lukas, 2003). AKT is the key factor in the phosphoinositide 3-kinase (PI3K) pathway and regulates the activation of the major signals for cell growth, survival, and metabolism (Carnero et al., 2008). To determine which factor is the downstream of DNA-PK in DMSR, G1 cells were pretreated with AKT, CHK1, or CHK2 inhibitor before IR treatment. DMSR was examined by microtubule regrowth assay 4 h after IR. AKT inhibition, but not CHK1 or CHK2 inhibition, resulted in an obvious decrease of DMSR (Fig. 6 A). Depletion of AKT affected DMSR (Fig. 6, B and C) and the accumulation of PCM proteins at the interphase centrosome after IR (Fig. 6 D), suggesting that AKT might be the downstream factor of DNA-PK after IR. We also confirmed the effect of AKT depletion on DMSR by a time-

lapse live-imaging experiment and found that loss of AKT led to decreased velocity of EB3 comets (Fig. 6 E) and the microtubule nucleation capacity of the centrosome (Fig. 6 F).

The phosphorylation of two key residues on AKT—Thr308 in the T-loop of the catalytic protein kinase core and Ser473 in a C-terminal hydrophobic motif—are required for AKT activation (Alessi et al., 1996). To determine the mechanism of AKT activation in DMSR, we separated cells into cytoplasmic and nuclear fractions. Nuclear pSer473 AKT increased after IR, which was consistent with previous reports. Intriguingly, in cytoplasmic fraction, pThr308 AKT, but not pSer473 AKT, significantly increased at 4 h after IR in G1 phase cells (Fig. 6 G). Cytoplasmic pThr308 signal increased at 2 h, peaked at 4 h, and started to decrease at 6 h after IR (Fig. 6 H), which was consistent with the time course of DMSR. Furthermore, DSB-induced cytoplasmic AKT Thr308 phosphorylation was abrogated by DNA-PK inhibition (Fig. 6 I). As PDK1 has been reported as the main protein kinase for pThr308 phosphorylation, we chemically inhibited PDK1 and found that, although the basal level of pThr308 AKT significantly decreased, the DSB-induced increase of cytoplasmic pThr308 AKT still existed (Fig. 6 J), indicating that DSB-induced pThr308 AKT is PDK1 independent. PDK1 inhibition did not affect DMSR (Fig. 6 K), implying that PDK1 is dispensable for DMSR. These results suggest that AKT could be the downstream factor of DNA-PK during DMSR.

As the importance of centrosome maturation on DMSR, we speculate that Thr308 phosphorylation may regulate DSB-induced interphase centrosome maturation and DMSR. Given that AKT has been reported to locate at the centrosome (Buttrick et al., 2008; Buttrick and Wakefield, 2008; Wakefield et al., 2003), we analyzed the effect of DMSR on the centrosomal localization of AKT. Although we could observe the centrosomal localization of AKT in RPE-1 cells, we encountered difficulties in quantitating the centrosomal AKT intensity due to high background of AKT immunofluorescence caused by the universal distribution of AKT in cytosol (Fig. S5 A). Thus, we could not draw a conclusion on the effect of DSBs on the accumulation of AKT on the centrosome. pT308 AKT has been reported to accumulate on mitotic centrosomes and regulate spindle assembly (Wakefield et al., 2003). Thus, we analyzed whether pThr308 AKT localized on the centrosome in interphase cells and found that pT308 AKT clearly located on the interphase centrosome and the signal increased at 4 h after IR in G1 cells (Fig. 7, A and B). Furthermore, DNA-PK inhibition could abolish the increase of pT308 AKT on the centrosome after IR, implying that DMSR resulted in the increased accumulation of pT308 AKT on the centrosome (Fig. 7, A and B). The fact that depletion of AKT eliminated the pT308 AKT signal on the centrosome (Fig. S5 B) suggested the specificity of the interphase centrosomal pT308

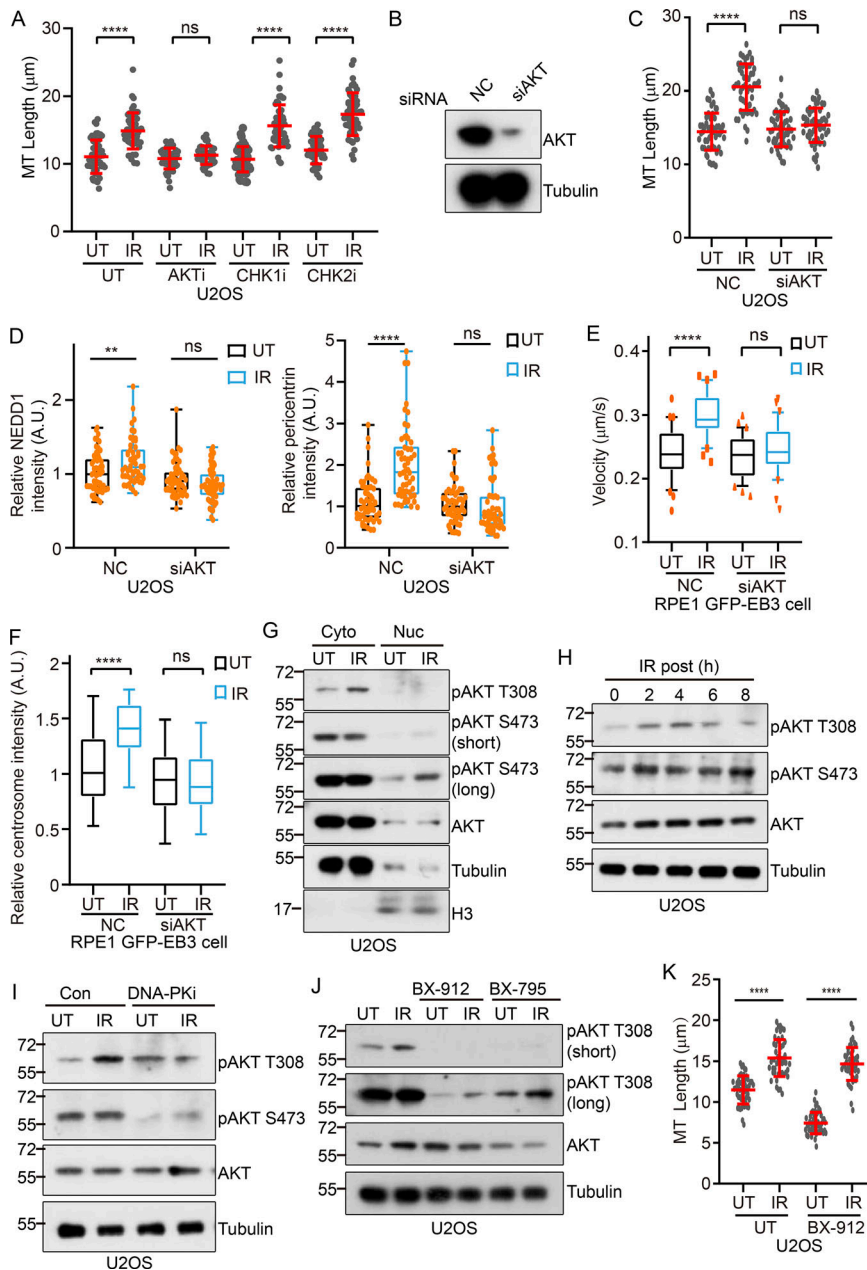


**Figure 6. AKT is involved in DMSR.** (A) G1 cells were preincubated with AKT, CHK1, and CHK2 inhibitors for 1 h and then treated with IR. DMSR was determined in these cells 4 h after IR. Quantitation of microtubule length is shown ( $n > 50$ ). (B) Western blot analysis showed the siAKT efficiency. (C) DMSR is inhibited by AKT depletion in G1 cells. Quantitation of microtubule length is shown ( $n > 50$ ). (D) Semi-quantitative analysis of relative NEDD1 or PCNT signal intensity at the centrosomes in G1 cells treated with scramble siRNA or siAKT is shown in box plot ( $n > 50$ ). (E) Quantitative analysis of GFP-EB3 comet velocity in siRNA-treated live GFP-EB3-expressing G1 cells is shown in box plot ( $n > 30$ ). (F) Quantitative analysis of relative centrosomal GFP-EB3 intensity in siRNA-treated live GFP-EB3-expressing G1 RPE-1 cells is shown in box plot ( $n > 30$ ). (G) IR treatment led to the increase of pT308 AKT signal in the cytoplasmic fraction, but not in the nuclear fraction. (H) Kinetics of IR-induced pT308 AKT. The pT308 AKT signal in the cytoplasmic fraction was determined by Western blot in G1 cells at indicated time points after 2 Gy IR. (I) DNA-PK inhibitor treatment attenuated IR-induced pT308 AKT. The cytoplasmic pT308 AKT was examined by anti-pT308 AKT antibody. (J) The cytoplasmic IR-induced pT308 AKT was examined in G1 U2OS cells after PDK1 inhibitors BX-912 or BX-795 treatment. (K) G1 cells were pretreated with BX-912 for 1 h and exposed to 2 Gy IR. DMSR was measured by microtubule regrowth assay ( $n > 50$ ). \*\*\*\*,  $P < 0.0001$ ; \*\*,  $P < 0.01$ ; ns, not significant. A.U., arbitrary units; MT, microtubule; UT, untreated.

AKT signal. Although PDK1 inhibition alone did not affect the DNA damage-induced accumulation of pT308 AKT signal on the interphase centrosome, PDK1 inhibition combined with DNA-PK inhibition greatly impaired the centrosomal localization of pT308 AKT (Fig. 7, C and D), indicating that DNA damage-induced accumulation of pT308 AKT on the interphase centrosome could be regulated by DNA-PK.

To explore how DNA-PK regulates the accumulation of pT308 AKT on the centrosome, we analyzed the cytoplasmic and nuclear distribution of DNA-PKcs and pS2056 DNA-PKcs after IR and found that both of them gradually increased after IR in the cytoplasmic portion of RPE-1 (Fig. 8 A) and HeLa cells (Fig. 8 B). Intriguingly, DNA damage-induced cytoplasmic pS2056 DNA-PKcs diminished in 53BP1-depleted cells, suggesting that 53BP1 may promote DMSR through regulating the cytoplasmic

distribution of activated DNA-PK. DMSR was affected when protein export was blocked by leptomycin B treatment (Fig. S5 C), implying the transportation of activated DNA-PK from nuclear to cytoplasm may be involved in DMSR. Moreover, we found that 53BP1 depletion abolished DNA damage-induced accumulation of pT308 AKT on the interphase centrosome, which is consistent with its role in the cytoplasmic distribution of activated DNA-PK (Fig. 8, C and D).

All these results implied that AKT was involved in DMSR and that DNA-PK may contribute to DSB-induced centrosomal accumulation of pThr308 AKT in G1 cells.

#### Centrosome integrity is critical for NHEJ repair

Microtubule dynamics promote DSB mobility through kinesins and the LINC complex, which is important for NHEJ repair

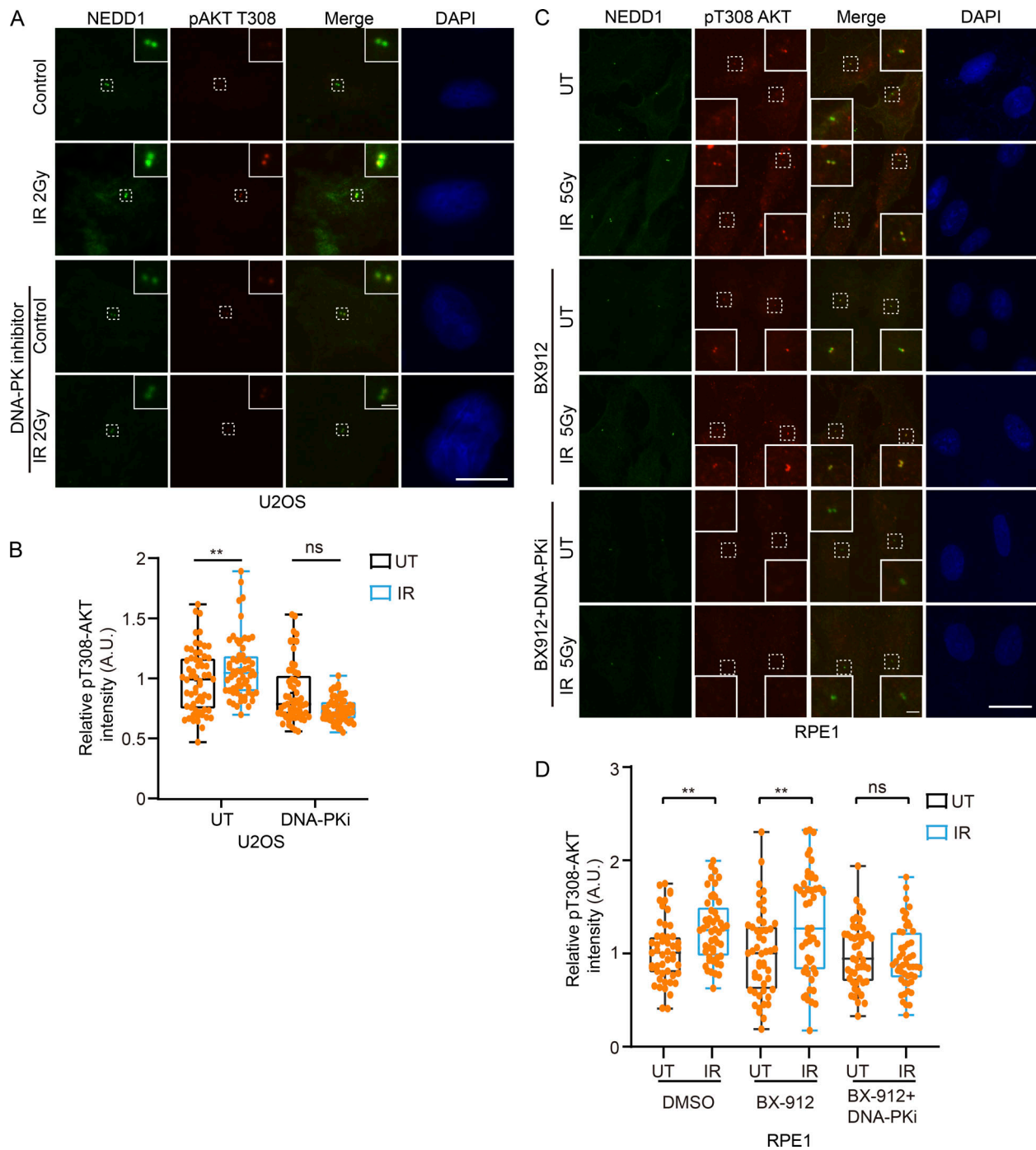


**Figure 7. DMSR led to accumulation of pT308 AKT on the centrosome. (A)** Upper: pT308 AKT colocalized with NEDD1 and increased after IR in G1 cells. Lower: DNA-PKcs inhibitor treatment inhibited the increase of pT308 on the centrosome after IR. **(B)** Box plot shows quantitation of the relative pT308 signal intensity at the centrosomes as assayed in A ( $n > 50$ ). **(C)** Upper: pT308 AKT colocalized with NEDD1 and the signal was increased after IR in G1 RPE1 cells. Middle: PDK1 inhibitor (BX-912) did not affect the IR-induced increase of pT308 AKT on the centrosomes. Lower: Cotreatment of DNA-PKcs inhibitor and PDK1 inhibitor (BX-912) inhibit the increase of pT308 after IR. **(D)** Quantitation of the relative pT308 signal intensity at the centrosome after indicated treatment is shown in box plot ( $n > 50$ ). Scale bar, 20 μm for labeled panels, 2 μm for magnified images. \*\*,  $P < 0.01$ ; ns, not significant. A.U., arbitrary units; UT, untreated.

(Lottersberger et al., 2015), implying that DMSR may function in DSB repair through regulating DSB mobility. First, we studied the role of DMSR on DSB mobility. As PCM proteins are important for DMSR, we depleted PCM proteins, such as PCNT and NEDD1, to abrogate DMSR and examined DSB mobility in these cells. As 53BP1 Tudor domain (TD) foci

(1220–1711 aa) have been widely used to measure the dynamics of DSBs (Li et al., 2019; Zgheib et al., 2009), we measured the mobility of GFP-53BP1 TD foci at 1 h after IR in G1 cells with indicated treatments. Nocodazole treatment, which could disassemble the microtubule network, significantly affected DSB mobility as shown by the ensemble mean-square

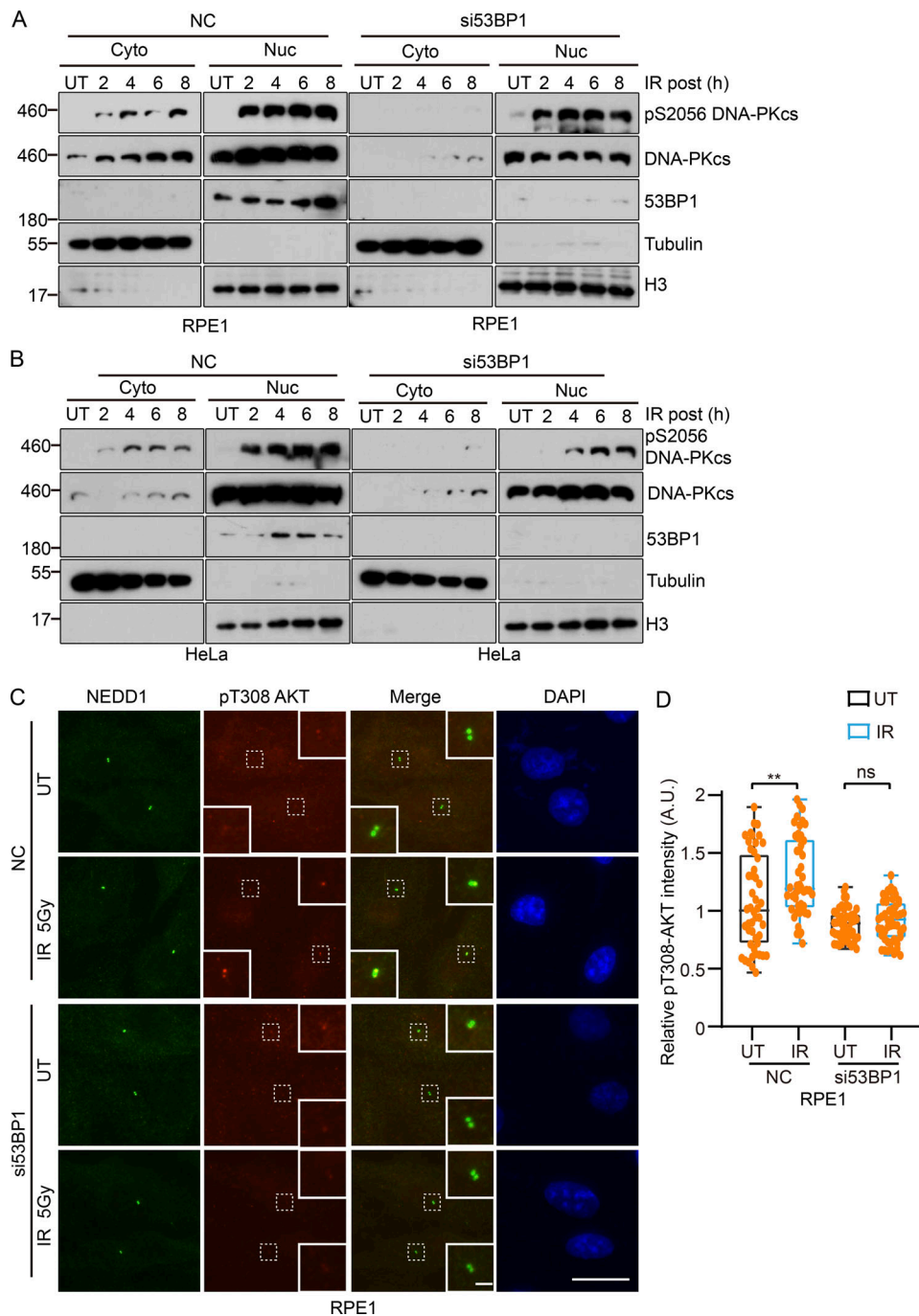
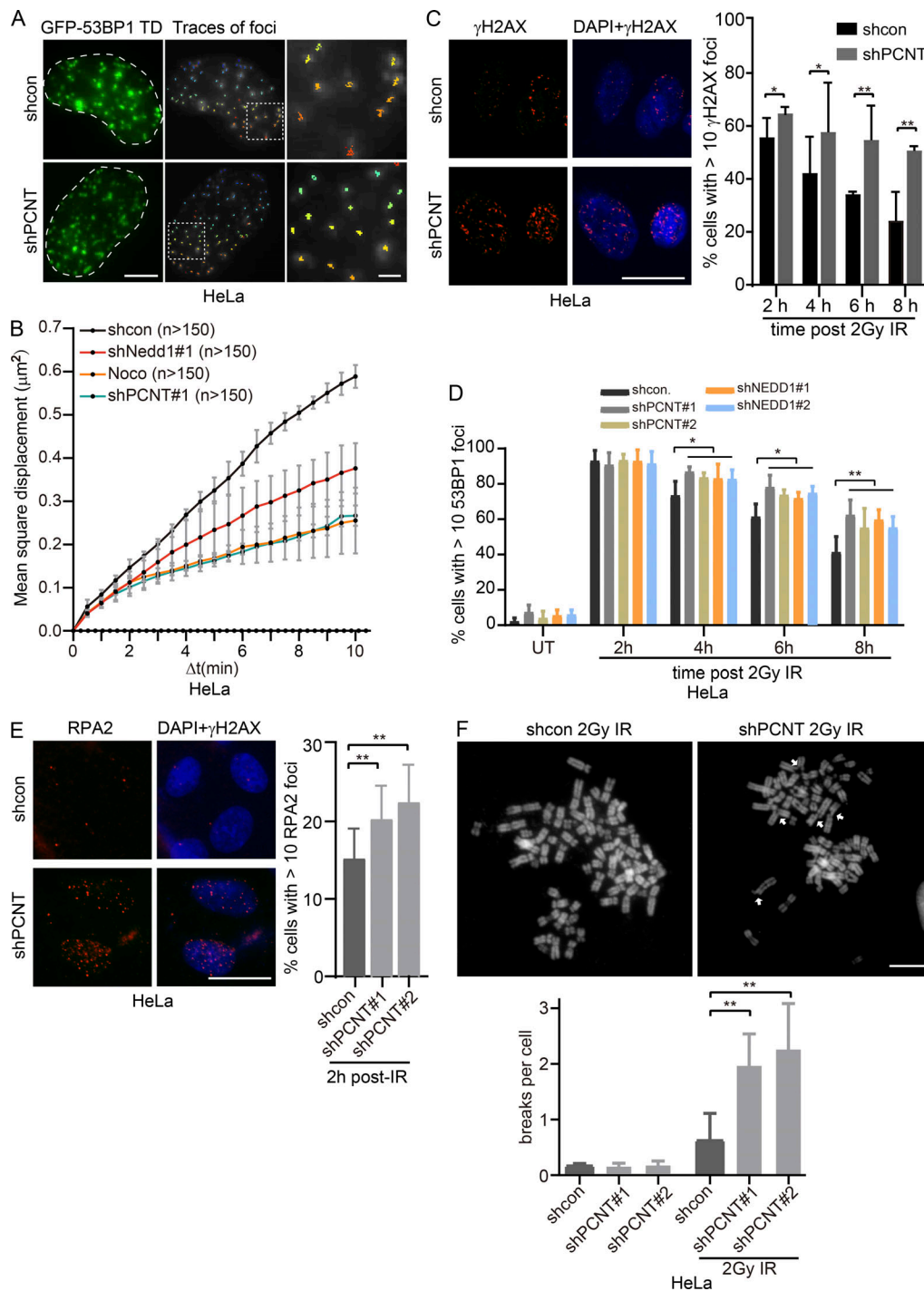


Figure 8. **53BP1 regulates IR-induced accumulation of pT308 AKT on the centrosomes.** (A and B) Control or si53BP1-treated G1 RPE-1 (A) or HeLa (B) cells were treated with 5 Gy IR. Cells were collected at indicated time points after IR and separated into cytoplasmic (Cyto) and nuclear (Nuc) fractions. Indicated proteins were analyzed by immunoblotting. (C) Upper: pT308 AKT colocalized with NEDD1, and the signal was increased after IR treatment in G1 RPE-1 cells. Lower: 53BP1 depletion inhibited the increase of pT308 after IR. Scale bar, 20  $\mu$ m for labeled panels, 2  $\mu$ m for magnified images. (D) Quantitation of the relative pT308 signal intensity at the centrosomes in NC or si53BP1 treated cells is shown in box plot ( $n > 50$ ). \*\*,  $P < 0.01$ ; ns, not significant. A.U., arbitrary units; UT, untreated.

displacement (eMSD) of 53BP1 foci in HeLa cells, which is consistent with a previous report (Fig. 9 B; Lottersberger et al., 2015). Interestingly, PCNT or NEDD1 knockdown decreased the DSB mobility as with nocodazole treatment (Fig. 9, A and B; and Videos 10 and 11), indicating that PCM proteins may contribute to DSB mobility in G1 cells. These

results demonstrated that PCM protein-dependent DMSR may regulate DSB mobility.

As DSB mobility contributes to the high efficiency of NHEJ, we speculated that DMSR contributed to c-NHEJ repair. As HeLa cells were used in previous reports to study end resection-dependent slow NHEJ (Barton et al., 2014; Biehs et al., 2017), we



**Figure 9. Centrosome integrity is important to DSB mobility and NHEJ repair.** (A) Examples of traces of GFP-53BP1TD foci in shcon or shPCNT G1 HeLa cells. Images were collected in cells expressing GFP-53BP1TD (residues 1220–1711) 1 h after IR (see also Videos 10 and 11). Scale bars, 10  $\mu\text{m}$  for labeled panel, 2  $\mu\text{m}$  for magnified images. (B) Nocodazole (Noco) treatment or depletion of PCNT or NEDD1 decreased DSB mobility. eMSD of the GFP-53BP1TD foci is shown in indicated conditions and for every time point. Values are shown as mean  $\pm$  SEM. The number of traces were pooled from three independent experiments. (C) Depletion of PCNT delayed NHEJ as determined by  $\gamma\text{H2AX}$  foci in different time points after IR. Left: Immunofluorescence showed  $\gamma\text{H2AX}$  foci in scramble shRNA- or shPCNT-treated G1 cells. Right: Quantitation of cells with  $\gamma\text{H2AX}$  foci in control or PCNT-depleted G1 cells at indicated time points ( $n > 50$ ). Scale bar, 20  $\mu\text{m}$ . (D) The kinetics of DNA damage repair in IR-treated G1 HeLa cells were determined by 53BP1 foci in shcon, shPCNT, or shNEDD1 cells ( $n > 100$ ). (E) RPA2 foci induced by IR increased in PCNT-depleted G1 HeLa cells. Left: RPA2 foci in control cells or PCNT-depleted cells. Right: Quantitation of cells with RPA2 foci in control cells or PCNT-depleted cells ( $n > 50$ ). Scale bar, 20  $\mu\text{m}$ . (F) Upper: Representative images showed chromosome breaks in shcon or shPCNT HeLa cells after IR. Arrow indicates chromosome breaks. Lower: Quantitation of chromosome breaks per cell in shcon or shPCNT cells with or without IR treatment ( $n > 30$ ). \*\*,  $P < 0.01$ ; \*,  $P < 0.05$ . UT, untreated.

employed HeLa cells in the following experiments to study the role of DMSR on c-NHEJ. First, we examined the NHEJ efficiency in G1 cells by  $\gamma$ H2AX immunofluorescence and found that, when cells were depleted with PCNT or NEDD1, the percentage of cells with >10  $\gamma$ H2AX foci was higher than that of control cells after IR, indicating that NHEJ efficiency was affected by PCNT (Fig. 9 C) or NEDD1 (Fig. S5 D) depletion. These results were confirmed by 53BP1 foci formation analysis in shPCNT and shNEDD1 G1 HeLa cells (Fig. 9 D and Fig. S5 E). c-NHEJ in G1 phase cells comprise a fast and a slow process and the latter depends on end resection. To determine whether the end resection process in slow NHEJ was also affected by PCNT depletion, RPA2, which coats single-strand DNA after end resection, was stained in synchronized G1/S HeLa cells at 2 h after IR. Intriguingly, the percentage of cells with RPA2 foci increased in PCNT-depleted (Fig. 9 E) or NEDD1-depleted cells (Fig. S5 D), indicating that, when fast NHEJ was affected, more DSBs were processed by end resection. These results suggest that, when DMSR was abolished through PCM protein depletion, the extent of end resection-dependent slow NHEJ increased in G1 cells. As slow NHEJ will cause genomic instability, we next examined the effect of PCM protein depletion on genomic instability. HeLa cells treated with scrambled shRNA, shPCNT, or shNEDD1 were synchronized in G1/S and exposed to 2 Gy IR, then released from double thymidine block. 8 h after IR, the cells were treated with nocodazole for 45 min to accumulate mitotic cells. Collected mitotic cells were analyzed by chromosome spread assay to calculate chromosome breaks. NEDD1 or PCNT depletion did not cause obvious chromosomal breaks in cells without IR treatment (Fig. 9 F and Fig. S5 F). Remarkably, IR treatment led to more chromosomal breaks in NEDD1- or PCNT-depleted cells than shcon (negative control scrambled shRNA) cells, indicating that DMSR may contribute to maintain genomic stability by facilitating c-NHEJ repair.

## Discussion

In this study, we uncovered that DSBs actively promote microtubule dynamics in G0/G1 cells through DMSR. DMSR is accompanied by PCM accumulation and interphase centrosome maturation, which required functional c-NHEJ, DNA-PK, and AKT. The 53BP1-Shieldin complex may also regulate DMSR through facilitating the activation of DNA-PK during c-NHEJ. DSB-induced interphase centrosome maturation leads to increased centrosome-dependent microtubule nucleation and polymerization, which could promote DSB mobility and facilitate c-NHEJ. Thus, we reveal a closed feedback loop between DSBs and microtubule dynamics during DSB repair (Fig. 10).

Several studies have reported the relationship between the centrosome and DNA damage. Most of them focused on the long-term effect of DNA damage, which induces centrosome over-duplication (Antonczak et al., 2016; Bourke et al., 2007; Dodson et al., 2004; Löffler et al., 2013; Mullee and Morrison, 2016; Sugihara et al., 2006). In this study, we uncovered DSB-induced short-term (within 6 h)- and cell phase (G1 or G0)-specific effects on the centrosome. Previous notions suggest that abnormal centrosomes lead to abnormal spindle assembly and

chromosomal separation in mitosis, which causes genomic instability (Mullee and Morrison, 2016). For example, PCNT mutations lead to genomic instability, and NEDD1 depletion results in cell senescence (Antonczak et al., 2016; Griffith et al., 2008; Manning and Kumar, 2010). Our study discovered that, during DMSR, both the rate of microtubule polymerization and the capacity of centrosome-dependent microtubule nucleation were promoted through DSB-induced accumulation of PCM proteins on centrosomes, which could promote DSB mobility and facilitate c-NHEJ repair. Thus, our new findings may provide a new explanation for these phenomena caused by centrosome protein defects.

DMSR is a short-term stress response and only occurs in G0/G1 cells, implying that DMSR is highly regulated. First, DMSR is restricted to 6 h after DNA damage. Microtubules are important cytoskeletons and usually serve as cargo transportation roads (Ross et al., 2008). Microtubules also play important roles in cell migration and the organization of many cellular components, including the ER and Golgi apparatus (Gurel et al., 2014). Prolonged changes in microtubule dynamics may affect the normal functions of these cellular apparatuses. Thus, the duration of DMSR should be restricted to a limited time period to avoid deleterious side effects. Second, DMSR happens specifically in G0/G1 cells, during which c-NHEJ is the predominant DSB repair pathway. Centrosome-dependent microtubule polymerization and nucleation capacity is weak in G1, while massive centrosome maturation happens at the G2/M transition for the following spindle formation in mitosis (Barr et al., 2004). In G1 cells, DSB-induced interphase centrosome maturation may be required for properly sustaining DSB mobility during c-NHEJ. In S/G2 phase, HR coexists with NHEJ, and elevated DSB mobility may cause genomic translocation (Li et al., 2019; Roukos et al., 2013). Thus, DMSR wisely disappears in S or G2 cells to balance the efficiency of NHEJ and accuracy of HR. Third, the mechanism of DSB-induced interphase centrosome maturation is different from the centrosome maturation in the G2/M transition. For instance, PLK1 is dispensable for DMSR. PLK1-dependent centrosome maturation may gradually become predominant from the G1 to G2 phase and compete with DNA-PK-AKT-mediated centrosome maturation. This may also explain why DMSR gradually disappears when cells enter S phase.

DSBs in G1 can be repaired by NHEJ in two ways: the fast NHEJ, which is an end resection-independent process, and slow NHEJ process, which is end resection dependent (Löbrich and Jeggo, 2017). Depletion of CtIP, EXO1, or Artemis, which is associated with slow NHEJ, does not affect DMSR, indicating that slow NHEJ is dispensable for DMSR. Instead, depletion of Ligase 4, XLF, or XRCC4, which are crucial for fast NHEJ, leads to persistent DMSR in G1, suggesting that a prolonged c-NHEJ process leads to overactivated DMSR. DMSR appears at around 1 h after DNA damage and diminishes at around 6 h, which overlaps with the fast NHEJ repair period (1–4 h after DNA damage; Löbrich and Jeggo, 2017). Furthermore, loss of DMSR by PCM protein depletion leads to increased end resection in G1, implying that DMSR may inhibit the end resection process in slow NHEJ by elevating DSB mobility. We hypothesize that, when fast NHEJ failed to repair DSBs properly in G1 cells, DMSR

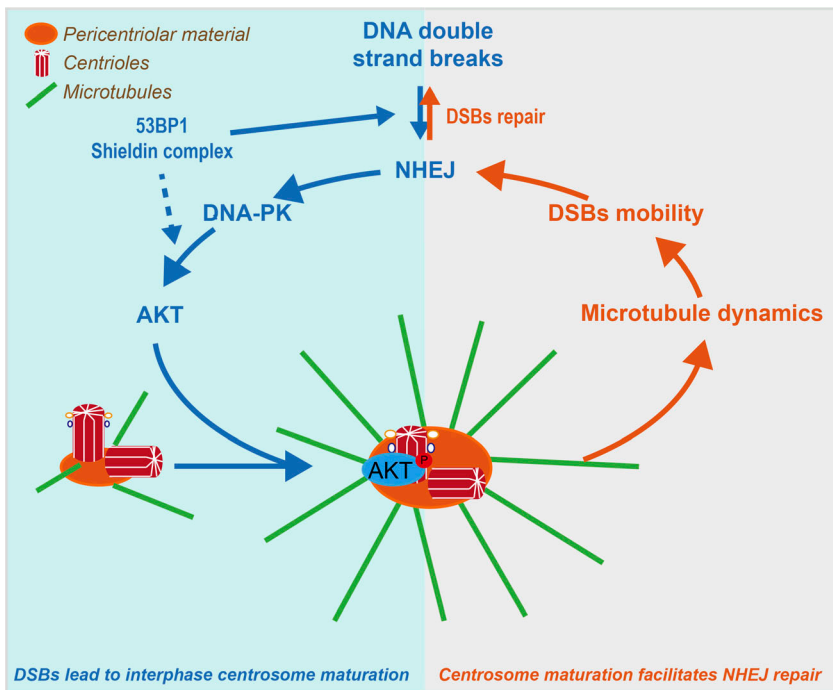


**Figure 10. Proposed model for DMSR.** DSBs are repaired by NHEJ repair process in G1 or G0 cells, which is accompanied by DNA-PK activation. Activated DNA-PK induces PCM accumulation at the centrosome and interphase centrosome maturation, during which pT308 AKT also accumulated on the centrosome. The 53BP1-Shieldin complex is involved in the regulation of this process (left). Elevated microtubule dynamics will promote DSB mobility, which facilitates the c-NHEJ repair (right).

could be activated to inhibit end resection and avoid slow NHEJ. Thus, DMSR may be important for maintaining genome stability in G1 cells through facilitating fast NHEJ.

DMSR is accompanied by pT308 AKT accumulation on interphase centrosomes. Although the localization of AKT and pT308 AKT on mitotic centrosomes has been reported (Buttrick et al., 2008; Buttrick and Wakefield, 2008; Wakefield et al., 2003), the localization of pT308 AKT on the interphase centrosome during DMSR is a novel finding. Interestingly, PDK1 is dispensable for DSB-induced interphase centrosomal accumulation of pThr308 AKT, which is consistent with the report that the localization of pT308 AKT on mitotic centrosomes is PI3K independent (Wakefield et al., 2003). Previous reports showed that both DNA-PK and ATM may contribute to Ser473 AKT phosphorylation (Bozulic et al., 2008; Fraser et al., 2011). Although we found that DNA-PK may contribute to the DMSR-related cytoplasmic pThr308 AKT, whether DNA-PK directly phosphorylates AKT on Thr308 is still unknown. It is also possible that DNA-PK may regulate the cytoplasmic distribution of pT308 AKT through phosphorylating AKT-binding proteins, or DNA-PK may phosphorylate AKT at other sites that facilitate the centrosomal accumulation of pT308 AKT. Further studies are needed to illustrate the relationship between DNA-PK and AKT during DMSR. As to how pT308 AKT regulates centrosome functions, several studies have reported that AKT could phosphorylate several substrates, including GSK-3 (Buttrick et al., 2008; Buttrick and Wakefield, 2008; Wakefield et al., 2003), TEF (Telomerase transcriptional element-interacting factor; Zhao et al., 2014), and Inversin (Suizu et al., 2016), to regulate interphase or mitotic centrosomes functions, respectively. Whether these AKT substrates are involved in DMSR and what is the exact role of pT308 AKT in DMSR still need further studies.

53BP1 has been proposed to promote DSB mobility to facilitate c-NHEJ repair, but the mechanism is still missing (Dimitrova et al., 2008; Lottersberger et al., 2015). In our study, we found that DNA-PK, 53BP1, and the Shieldin complex were important regulators of DMSR. Inhibition of DNA-PK abolished the S2056 phosphorylation of human DNA-PKcs, suggesting S2056 is the autophosphorylation site (Chen et al., 2005). Thus, pS2056 has been widely used as the marker for DNA-PKcs activation. By probing pS2056 DNA-PKcs, we found that DNA-PK activation was delayed in both cytoplasmic and nuclear fractions in 53BP1-depleted G1 HeLa and RPE-1 cells after IR. Thus, 53BP1 may contribute to DMSR through facilitating DNA-PK activation. We hypothesize that the increase of the 5' end resection in 53BP1-depleted G1 cells may switch off DNA-PK and subsequently DMSR, which might lead to precocious activation of slow NHEJ. We also found that, although at a relatively lower level, the activation of DNA-PK (pS2056) still could be observed in 53BP1-depleted G1 cells after IR. One possibility is that when 53BP1 is depleted, end resection happens in a subset of DSBs, and DNA-PK still could be activated by the remaining unresected DSBs, which leads to a decreased DNA-PK activation and defective DMSR. Interestingly, although 53BP1/Rif1/Shieldin could inhibit 5' end resection at DSBs to promote c-NHEJ, 53BP1, but not Rif1 and Rev7, is required for DSB mobility (Boersma et al., 2015; Zimmermann et al., 2013). Meanwhile, Dimitrova et al. (2008) reported that both ATM and 53BP1 are required for the increased telomere mobility after their deprotection. On the contrary, our data show that DMSR depends on DNA-PK but not ATM, and DMSR also could be affected by Rev7 depletion. These discrepancies suggest that DSB mobility may be regulated by several different pathways, and more evidence is needed to illustrate the regulation and function of DSB mobility in the future.

Another remaining question is how signals from nuclear DDR are transported to the cytoplasmic centrosome. DNA-PKcs could locate in both the nucleus and cytoplasm (Poruchynsky et al., 2015; Saji et al., 2005; Wang et al., 2013). It is possible that activated DNA-PKcs is exported from nucleus to cytoplasm after IR and subsequently transported to the centrosome through microtubules during DMSR. In fact, microtubule localization of DDR-related proteins, including DNA-PKcs, has been observed (Poruchynsky et al., 2015). Disruption of nuclear export by leptomycin B treatment abolishes DMSR, implying that nuclear export might play a role in DMSR.

Gene transcription in normal cells could induce massive endogenous DSBs, which are mainly repaired by c-NHEJ (Dellino et al., 2019). The elegantly regulated DMSR revealed an underlying relationship between DSBs and the centrosomes in quiescent (G<sub>0</sub>) and nontransformed (RPE-1) interphase cells. Aberrant centrosomes may affect c-NHEJ repair of endogenous DSBs generated from transcription in normal cells or end-differentiated cells, which may lead to cancer-associated genome instability. Thus, our findings may shed light on the explanation of the cancerous transition of end-differentiated cells.

## Materials and methods

### Microtubule regrowth assay

Cells were grown on coverslips and treated with cold medium on ice for 30 min to depolymerize microtubules. Microtubule regrowth was allowed in prewarmed medium for 1 or 2 min (as indicated in figures) in 37°C. Cells were fixed with PHEM buffer (Pipes 60 mM, Hepes 25 mM, EGTA 10 mM, MgCl<sub>2</sub> 2 mM, pH 6.9) containing 4% PFA and 0.5% Triton X-100 for 15 min at room temperature. After washing several times with PBS, cells were stained with anti-β-tubulin (Frbio; 1:200) antibody. Images were gathered through Z-stack by Olympus IX83 microscopy and Andor's Zyla 5.5 camera, and deconvolution analysis was done by cellSens software. Z-stacks at 0.34-μm steps were acquired by Olympus with 60× oil objective lens (NA, 1.35). For measuring the microtubule length in each microtubule regrowth experiment, three microtubules in each cell were counted and the average value was used as the microtubule length for the cell. More than 50 cells were measured for each sample in all the experiments. Quantitation of the microtubule length in each experiment was repeated by three members in the laboratory and we got the same tendency. The quantitative results from one person were shown in each figure. All statistical analysis was done using GraphPad Prism 8 software.

### Immunofluorescence and quantitation of fluorescence intensity

For centrosome-associated protein immunofluorescence, U2OS cells were grown on glass coverslips and fixed and permeabilized in methanol for 5 min. For phospho-AKT (Thr308), γH2AX, and RPA2, U2OS cells were permeabilized with 0.5% Triton X-100 for 5 min, then fixed in methanol for 5 min. The fixed coverslips were incubated with primary antibodies in PBS with 1% BSA at 37°C for 1 h, then washed three times with PBS. Cells were then incubated with secondary antibodies for 1 h at

37°C and stained with Hoechst33342 or DAPI. Digital images were captured on an Olympus IX83 microscopy with 60× oil objective lens (NA, 1.35) and Andor's Zyla 5.5 sCMOS camera and cellSens Dimension software in the same exposure time in each experiment. For quantitation of the centrosome-related protein fluorescence intensity, the fluorescence image was registered and converted to gray 8-bit, and centrosome particles were measured by using the Particles Analysis function of ImageJ. The concentration of primary antibodies we used for immunofluorescence is: anti-β-tubulin (Frbio; 1:200); anti-γ-tubulin, anti-RPA2, and anti-DNA-PKcs (Proteintech; 1:100); anti-NEDD1 (Abcam; 1:50); anti-pericentrin and γH2AX (Abcam; 1:500); anti-CEP170 (Proteintech; 1:200); anti-NINEIN (ABclonal; 1:300); anti-53BP1 (Cell Signaling Technology [CST]; 1:500); anti-AKT1 (Proteintech; 1:50); and anti-pT308 AKT, anti-pT473 AKT, and anti-pS8-RPA2 (CST; 1:100). The secondary antibodies TRITC-Rb/M and FITC-Rb/M were purchased from Jackson ImmunoResearch, and the using concentration is 1:300.

### Chromosome spread

HeLa cells were synchronized in G<sub>1</sub>/S phase by double thymidine and treated with 2 Gy IR. After washing three times with PBS, cells were cultured in fresh medium for 8 h to allow cells to enter mitosis. Cells were then treated with 330 μM nocodazole for 45 min to harvest mitotic cells. Mitotic cells were collected and dehydrated with 55 mM KCl for 20 min at 37°C, prefixed with 40% fixative (methanol/acetic acid, 3:1) for 5 min, and centrifuged at 500 g for 5 min. After removing supernatant, cells were fixed twice by fixative at room temperature for 30 min, then cell suspension was dropped on the slide. The slide with spread chromosomes was dried at room temperature and stained with 1 μg/ml Hoechst33342 for 10 min.

### Cell cycle synchronization and analysis

U2OS, HeLa, RPE-1, and MCF7 cells were synchronized in G<sub>1</sub>/S by double thymidine treatment. Briefly, cells were treated with 2.5 μM thymidine for 16 h, washed three times with PBS, and cultured with fresh medium for 9 h. Cells were then treated with 2.5 μM thymidine for another 16 h to allow cells to be blocked in G<sub>1</sub>/S phase. For G<sub>0</sub> phase, U2OS or RPE-1 cells were treated by serum starvation for 40 h.

For cell cycle analysis, cells were synchronized, collected using pancreatic enzyme, and washed in PBS. Cells were fixed in cold 70% ethanol overnight at 4°C, spun at 500 g in a centrifuge, and the supernatant carefully discarded. Then the cell pellet was washed two times by PBS. To stain DNA, the cell pellet was resuspended with PBS containing 50 μg/ml propidium iodide, 100 μg/ml RNaseA, 0.2% Triton X-100, and incubated at 4°C for 30 min. Stained cells were sent to flow cytometry (BD; LSRFortessaX20), and cell cycle was analyzed by using FlowJo software.

### Cell culture, IR treatment, and chemical treatment

U2OS, RPE-1, HeLa, and 293T cells were cultured in DMEM containing 10% FBS and 1% penicillin/streptomycin at 37°C and 5% CO<sub>2</sub>. For microtubule regrowth assay, centrosomal protein immunofluorescence, and pS2056 DNA-PKcs analysis, U2OS or RPE-1 cells were irradiated with 2 Gy or 5 Gy and recovered for



different time points (1, 2, 4, 6, and 8 h). For pT308/S473 AKT analysis, RPE-1 cells were exposed to 10 Gy IR. For chromosome spread, HeLa cells were exposed to 2 Gy IR. The following chemicals were used: DNA-PKcs inhibitor (MCE; ku57788; 1  $\mu$ M), ATM inhibitor (MCE; ku55933; 10  $\mu$ M), ATR inhibitor (MCE; ADZ6783; 1  $\mu$ M), AKT inhibitor (TargetMol; MK-2206; 5  $\mu$ M), CHK1 inhibitor (MCE; SB 218078; 10  $\mu$ M), CHK2 inhibitor (MCE; CCT241533 hydrochloride; 5  $\mu$ M), PLK1 inhibitor (MCE; BI2536; 100 nM), p38/MAPK inhibitor (MCE; SB 203580; 10  $\mu$ M), PDK1 inhibitor (MCE; BX-795, 10  $\mu$ M; BX-912, 10  $\mu$ M), bleomycin (MCE; 5  $\mu$ g/ml), mitomycin C (MCE; MMC, 5  $\mu$ M), camptothecin (Sigma; CPT, 1  $\mu$ M), cisplatin (Sigma; 2.5  $\mu$ M), and etoposide (Sigma; 1  $\mu$ M). For microtubule regrowth assay and immunofluorescence, cells were preincubated with indicated inhibitors for 1 h before DNA damage treatment. For Western blot analysis of AKT phosphorylation, cells were preincubated with DNA-PKcs inhibitor for 3 h or PDK1 inhibitor for 1 h before IR treatment.

### RNAi transfection and quantitative RT-PCR

For RNAi experiments, siRNAs were transfected into U2OS or RPE-1 cells using Lipofectamine RNAiMAX according to manufacturer's instructions (Invitrogen). Cells were synchronized in G1/S phase by double thymidine treatment after 8 h transfection, or cells were collected and analyzed by quantitative RT-PCR or Western blot after 48-h transfections to determine the knockdown efficiency. As an NC, cells were also transfected with an equal amount of scrambled siRNA (NC siRNA) or scrambled shRNA (NC shRNA). The target sequence of each siRNA or shRNA is listed in Table S1. The effect of gene depletion was examined by Western blot or quantitative RT-PCR, and most of the results are shown in Fig. S3.

For quantitative RT-PCR, total RNA was extracted by using the Trizol RNA extraction protocol. One microgram of total RNA was reverse transcribed into cDNA by using the HIScriptII One Step RT-PCR Kit (Vazyme). Gene expression was analyzed by real-time quantitative PCR by using the SYBR Green quantitative PCR Mix (Monad) real-time PCR system. PCR reaction ran for 40 cycles at 95°C for 5 s, 60°C for 1 min, and 72°C for 30 s. Each cDNA sample was run with triplicates. The mRNA level of each sample for each gene was normalized to that of the GAPDH mRNA. The relative mRNA level was presented as unit values of  $2^{-(Ct[GAPDH]-Ct[\text{gene of interest}]})$ .

### Transfection, lentivirus package, and infection

Transient plasmids transfection was performed with polyethylenimine. For the lentivirus package, shRNA plasmids and lentivirus plasmids (pSPAX2 and pMD2G) were cotransfected into 293T cells using polyethylenimine. After 56-h transfections, the supernatants containing packaged lentivirus were harvested to infect HeLa cells with 8  $\mu$ g/ml polybrene. Stable cell pools were selected in medium containing 2  $\mu$ g/ml puromycin.

### Dynamics of GFP-EB3

To measure the speed of microtubule growth in live cells, RPE-1 cells stably expressing GFP-EB3 were seeded to a 20-mm glass culture dish in DMEM with 10% FBS and synchronized in G1/S

phase by double thymidine block. Imaging was gathered using Airyscan of Zeiss LSM880 confocal with 63 $\times$  oil objective lens (NA, 1.4) equipped with an environment chamber at 37°C and ZEN (black) gathering software. Time-lapse images were acquired with 1.3 pinhole and 1-s interval per frame over 30 s with 512  $\times$  512 pixels in final size. To track the trajectory and analyze the movement velocity of GFP-EB3, ImageJ software with the Kymograph plug-in was used as described (Mangeol et al., 2016). These images within 30 s were used to make maximum intensity projections by KymographClear and got the overlaid images. Briefly, a series of images from each time-lapse experiment was opened by ImageJ with KymographClear, and images captured at different time points were overlaid to define the tracks of GFP-EB3 comets movement. Tracking diagrams were made using the Manual Tracking plug-in for ImageJ software and Adobe Photoshop, and the movies of the overlaid images were made by Adobe Premiere. Quantitative velocity measurements of the distribution of EB3-GFP tracks were done by plotting the average pixel intensities along a thick line with the width of 5 pixels using normalized projection images spanning 30 s in ImageJ software with the KymographDirect plug-in. The following parameters were used in KymographDirect: time per frame = 1,000 ms; pixel size = 100 nm; particle width = 3 pixels; maximum number of intermediate lines = 100; search window width = 2; and line width = 5 pixels. Finally, the forward motion of each kymograph was analyzed using a noise-reduction algorithm with a 0.5 intensity threshold under the above KymographDirect parameters. Statistical analyses were performed by using an unpaired two-tailed Student's *t* test using GraphPad Prism software. Each experiment was repeated three times and one representative quantitative result from these experiments is shown in the figures.

### DSB mobility analysis by GFP-53BP1 TD

To analyze the DSB mobility, PCNT- or NEDD1-depleted HeLa cells were transfected with GFP-53BP1 TD plasmids. Cells were cultured in DMEM with 10% FBS. After synchronization in G1/S by double thymidine, cells were treated with 2 Gy IR. Imaging was gathered using Olympus IX83 microscopy (Olympus America) with 60 $\times$  oil objective lens (NA, 1.35) and Andor's Zyla 5.5 sCMOS camera and cellSens Dimension software at 1 h after IR. The IR-induced DSB mobility was analyzed following the basic procedures described in a previous report (Lottersberger et al., 2015). Briefly, 5- $\mu$ m Z-stacks at 0.5- $\mu$ m step images were acquired with 50-ms exposure time every 30 s per frame over 10 min with 2056  $\times$  2056 pixels in final size. After deconvolution, image stacks were average projected. To get the track of 53BP1 foci in different treatment conditions, cells were registered by the tracking plugin with ImageJ, and then particles were detected by the LoG Detector and tracked using TrackMate plugin.

The position *r* from the same molecule in adjacent frames in the same cells were linked by standard algorithms using Trackpy, from which the trajectories of individual molecules (*t*) were obtained. The eMSD of every 53BP1 foci in cells was calculated by Python tracking packing Trackpy using the following equation:  $[\Delta r^2(\tau)] = [(r(t + \tau) - r(t))^2]$ . The eMSD data were then

averaged from multiple movies for the same sample at the same time point (<http://soft-matter.github.io/trackpy/v0.4.2/>).

### Nuclear and cytoplasmic protein extraction and Western blot

For distinguishing phosphorylation of AKT in the nuclear and cytoplasmic fraction, RPE-1 cells were collected and extracted by using a nuclear and cytoplasmic protein extraction kit (Beyotime; P0027), according to the manufacturer's instructions. Briefly, cells were collected by PBS that contained 10 mM EDTA and washed one time by PBS. Cells were lysed in ice-cold cytoplasmic protein extraction fraction A for 15 min and centrifuged at 15,000 *g* for 5 min; the supernatant fraction was cytoplasmic protein. The pellet was then resuspended in the ice-cold nuclear protein extraction buffer by vortexing, incubated on ice for 30 min and centrifuged at 15,000 *g* for 10 min; the supernatant fraction was the nuclear protein. To quantify protein concentration, a BCA kit for protein determination (ZOMANBIO; ZD301-2) was used. For the Western blot assays, the proteins were separated by SDS-PAGE and transferred onto polyvinylidene difluoride membranes (Millipore). The membranes were blocked with 5% milk in PBST (PBS with Tween 20), probed with primary and then secondary antibodies, and finally exposed using ECL (Bio-Rad; US EVERBRIGHT). The concentration of primary antibodies AKT1,  $\beta$ -tubulin,  $\beta$ -actin, pericentrin, and 53BP1 was 1:3,000, and the concentration of another primary antibody was 1:1,000. The secondary antibody HRP-Rb/M was purchased from Jackson ImmunoResearch and the concentration was 1:20,000.

### Statistical analysis

All statistical induction and statistical analysis were done using GraphPad Prism software. Mean values were compared by *t* tests and nonparametric tests for the variance analysis between different groups. Differences were considered significant for *P* values < 0.05 (\*\*\*\*, *P* < 0.0001; \*\*\*, *P* < 0.001; \*\*, *P* < 0.01; \*, *P* < 0.05; mean  $\pm$  SD). All the experiments were repeated three times. For the results shown in box plots when PCM protein intensity was analyzed: center line, median; box limits, 25th and 75th percentile; whiskers, maximum and minimum. When GFP-EB3 velocity and intensity was analyzed: center line, median; box limits, 25th and 75th percentile; whiskers, fifth and 95th percentile.

### Online supplemental material

Fig. S1 contains the experiment procedure for Fig. 1 A and supporting images for Fig. 2. Fig. S2 summarizes the experiment procedures for Fig. 3, A and B, and Fig. 3 D. Fig. S3 contains supporting information for Fig. 4, including Western blots showing the efficiency of indicated siRNA and typical images showing DMSR under indicated conditions. Fig. S4 shows the supporting data for Fig. 5, including the centrosomal accumulation of Ninein and CEP170 during DMSR. Fig. S5 contains supportive data for Fig. 6 and additional images of 53BP1 foci images for Fig. 7. Videos 1, 2, and 3 correspond to Fig. 2 A, showing the GFP-EB3 comet movement under indicated treatment. Videos 4, 5, 6, and 7 correspond to Fig. 2 C, showing the GFP-EB3 movement. Videos 8 and 9 correspond to Fig. 2 E,

showing the GFP-EB3 in untreated (Video 8) and bleomycin-treated (Video 9) G1 RPE-1 cells. Videos 10 and 11 correspond to Fig. 9 A, showing the DSB mobility through GFP-53BP1TD foci in shcon (Video 10) or shPCNT (Video 11) G1 HeLa cells. Table S1 contains the sequence information for siRNA or shRNA and the catalog number for the chemicals used in this study.

### Acknowledgments

We thank Jiwei Chang (Medical Research Institute, Wuhan University, Wuhan, China) for the help on data analysis.

This work was supported by grants from the National Key Research and Development Program of China (2018YFC1003400), the National Natural Science Foundation of China (31770868), Wuhan University (2042018kf0215), and the Medical Science Advancement Program (Basic Medical Sciences) of Wuhan University (TFJC2018005) to Q. Chen.

The authors declare no competing financial interests.

Author contributions: Q. Chen and X. Zhang designed and supervised the study; S. Ma performed the experiments and data analysis; C. Liu and Z. Rong generated constructs; C. Liu, Z. Rong, and X. Qin contributed to the statistical analysis; Q. Chen, X. Zhang, and S. Ma wrote the paper.

Submitted: 6 November 2019

Revised: 1 November 2020

Accepted: 2 December 2020

### References

- Alessi, D.R., M. Andjelkovic, B. Caudwell, P. Cron, N. Morrice, P. Cohen, and B.A. Hemmings. 1996. Mechanism of activation of protein kinase B by insulin and IGF-1. *EMBO J.* 15:6541–6551. <https://doi.org/10.1002/j.1460-2075.1996.tb01045.x>
- Antonczak, A.K., L.I. Mullee, Y. Wang, D. Comartin, T. Inoue, L. Pelletier, and C.G. Morrison. 2016. Opposing effects of pericentrin and microcephalin on the pericentriolar material regulate CHK1 activation in the DNA damage response. *Oncogene.* 35:2003–2010. <https://doi.org/10.1038/onc.2015.257>
- Barr, F.A., H.H. Siljé, and E.A. Nigg. 2004. Polo-like kinases and the orchestration of cell division. *Nat. Rev. Mol. Cell Biol.* 5:429–440. <https://doi.org/10.1038/nrml401>
- Bartek, J., and J. Lukas. 2003. Chk1 and Chk2 kinases in checkpoint control and cancer. *Cancer Cell.* 3:421–429. [https://doi.org/10.1016/S1535-6108\(03\)00110-7](https://doi.org/10.1016/S1535-6108(03)00110-7)
- Barton, O., S.C. Naumann, R. Diemer-Biehs, J. Kunzel, M. Steinlage, S. Conrad, N. Makharashvili, J. Wang, L. Feng, B.S. Lopez, et al. 2014. Polo-like kinase 3 regulates CtIP during DNA double-strand break repair in G1. *J. Cell Biol.* 206:877–894. <https://doi.org/10.1083/jcb.201401146>
- Biehs, R., M. Steinlage, O. Barton, S. Juhasz, J. Kunzel, J. Spies, A. Shibata, P.A. Jeggo, and M. Lobrich. 2017. DNA Double-Strand Break Resection Occurs during Non-homologous End Joining in G1 but Is Distinct from Resection during Homologous Recombination. *Mol. Cell.* 65:671–684.e5.
- Boersma, V., N. Moatti, S. Segura-Bayona, M.H. Peuscher, J. van der Torre, B.A. Wevers, A. Orthwein, D. Durocher, and J.J.L. Jacobs. 2015. MAD2L2 controls DNA repair at telomeres and DNA breaks by inhibiting 5' end resection. *Nature.* 521:537–540. <https://doi.org/10.1038/nature14216>
- Bourke, E., H. Dodson, A. Merdes, L. Cuffe, G. Zachos, M. Walker, D. Gillespie, and C.G. Morrison. 2007. DNA damage induces Chk1-dependent centrosome amplification. *EMBO Rep.* 8:603–609. <https://doi.org/10.1038/sj.embor.7400962>
- Bozulic, L., B. Surucu, D. Hynx, and B.A. Hemmings. 2008. PKBalpha/Akt1 acts downstream of DNA-PK in the DNA double-strand break response and promotes survival. *Mol. Cell.* 30:203–213. <https://doi.org/10.1016/j.molcel.2008.02.024>

- Buttrick, G.J., and J.G. Wakefield. 2008. PI3-K and GSK-3: Akt-ing together with microtubules. *Cell Cycle*. 7:2621–2625. <https://doi.org/10.4161/cc.7.17.6514>
- Buttrick, G.J., L.M. Beaumont, J. Leitch, C. Yau, J.R. Hughes, and J.G. Wakefield. 2008. Akt regulates centrosome migration and spindle orientation in the early *Drosophila melanogaster* embryo. *J. Cell Biol.* 180:537–548. <https://doi.org/10.1083/jcb.200705085>
- Caridi, C.P., C. D'Agostino, T. Ryu, G. Zapotoczny, L. Delabaere, X. Li, V.Y. Khodaverdian, N. Amaral, E. Lin, A.R. Rau, and I. Chiolo. 2018. Nuclear F-actin and myosins drive relocalization of heterochromatic breaks. *Nature*. 559:54–60. <https://doi.org/10.1038/s41586-018-0242-8>
- Carnero, A., C. Blanco-Aparicio, O. Renner, W. Link, and J.F. Leal. 2008. The PTEN/PI3K/AKT signalling pathway in cancer, therapeutic implications. *Curr. Cancer Drug Targets*. 8:187–198. <https://doi.org/10.2174/156800908784293659>
- Chen, B.P., D.W. Chan, J. Kobayashi, S. Burma, A. Asaithamby, K. Morotomi-Yano, E. Botvinick, J. Qin, and D.J. Chen. 2005. Cell cycle dependence of DNA-dependent protein kinase phosphorylation in response to DNA double strand breaks. *J. Biol. Chem.* 280:14709–14715. <https://doi.org/10.1074/jbc.M408827200>
- Colello, D., S. Mathew, R. Ward, K. Pumiglia, and S.E. LaFlamme. 2012. Integrins regulate microtubule nucleating activity of centrosome through mitogen-activated protein kinase/extracellular signal-regulated kinase/extracellular signal-regulated kinase (MEK/ERK) signaling. *J. Biol. Chem.* 287:2520–2530. <https://doi.org/10.1074/jbc.M111.254128>
- Dellino, G.I., F. Palluzzi, A.M. Chiariello, R. Piccioni, S. Bianco, L. Furia, G. De Conti, B.A.M. Bouwman, G. Melloni, D. Guido, et al. 2019. Release of paused RNA polymerase II at specific loci favors DNA double-strand-break formation and promotes cancer translocations. *Nat. Genet.* 51:1011–1023. <https://doi.org/10.1038/s41588-019-0421-z>
- Dev, H., T.W. Chiang, C. Lescale, I. de Krijger, A.G. Martin, D. Pilger, J. Coates, M. Sczaniecka-Clift, W. Wei, M. Ostermaier, et al. 2018. Shieldin complex promotes DNA end-joining and counters homologous recombination in BRCA1-null cells. *Nat. Cell Biol.* 20:954–965. <https://doi.org/10.1038/s41556-018-0140-1>
- Dimitrova, N., Y.C. Chen, D.L. Spector, and T. de Lange. 2008. 53BP1 promotes non-homologous end joining of telomeres by increasing chromatin mobility. *Nature*. 456:524–528. <https://doi.org/10.1038/nature07433>
- Dodson, H., E. Bourke, L.J. Jeffers, P. Vagnarelli, E. Sonoda, S. Takeda, W.C. Earnshaw, A. Merdes, and C. Morrison. 2004. Centrosome amplification induced by DNA damage occurs during a prolonged G2 phase and involves ATM. *EMBO J.* 23:3864–3873. <https://doi.org/10.1038/sj.emboj.7600393>
- Dodson, H., S.P. Wheatley, and C.G. Morrison. 2007. Involvement of centrosome amplification in radiation-induced mitotic catastrophe. *Cell Cycle*. 6:364–370. <https://doi.org/10.4161/cc.6.3.3834>
- Escribano-Díaz, C., A. Orthwein, A. Fradet-Turcotte, M. Xing, J.T. Young, J. Tkáč, M.A. Cook, A.P. Rosebrock, M. Munro, M.D. Canny, et al. 2013. A cell cycle-dependent regulatory circuit composed of 53BP1-RIF1 and BRCA1-CtIP controls DNA repair pathway choice. *Mol. Cell*. 49:872–883. <https://doi.org/10.1016/j.molcel.2013.01.001>
- Findlay, S., J. Heath, V.M. Luo, A. Malina, T. Morin, Y. Coulombe, B. Djerir, Z. Li, A. Samiei, E. Simo-Cheyrou, et al. 2018. SHLD2/FAM35A co-operates with REV7 to coordinate DNA double-strand break repair pathway choice. *EMBO J.* 37:e100158. <https://doi.org/10.15252/embj.2018100158>
- Fraser, M., S.M. Harding, H. Zhao, C. Coackley, D. Durocher, and R.G. Bristol. 2011. MRE11 promotes AKT phosphorylation in direct response to DNA double-strand breaks. *Cell Cycle*. 10:2218–2232. <https://doi.org/10.4161/cc.10.13.16305>
- Ghezaoui, H., C. Oliveira, J.R. Becker, K. Bilham, D. Moralli, C. Anzilotti, R. Fischer, M. Deobagkar-Lele, M. Sanchiz-Calvo, E. Fueyo-Marcos, et al. 2018. 53BP1 cooperation with the REV7-shieldin complex underpins DNA structure-specific NHEJ. *Nature*. 560:122–127. <https://doi.org/10.1038/s41586-018-0362-1>
- Griffith, E., S. Walker, C.A. Martin, P. Vagnarelli, T. Stiff, B. Vernay, N. Al Sanna, A. Sagar, B. Hamel, W.C. Earnshaw, et al. 2008. Mutations in pericentrin cause Seckel syndrome with defective ATR-dependent DNA damage signaling. *Nat. Genet.* 40:232–236. <https://doi.org/10.1038/ng.2007.80>
- Gupta, R., K. Somyajit, T. Narita, E. Maskey, A. Stanlie, M. Kremer, D. Typas, M. Lammers, N. Mailand, A. Nussenzweig, et al. 2018. DNA Repair Network Analysis Reveals Shieldin as a Key Regulator of NHEJ and PARP Inhibitor Sensitivity. *Cell*. 173:972–988.e23.
- Gurel, P.S., A.L. Hatch, and H.N. Higgs. 2014. Connecting the cytoskeleton to the endoplasmic reticulum and Golgi. *Curr. Biol.* 24:R660–R672. <https://doi.org/10.1016/j.cub.2014.05.033>
- Hauer, M.H., and S.M. Gasser. 2017. Chromatin and nucleosome dynamics in DNA damage and repair. *Genes Dev.* 31:2204–2221. <https://doi.org/10.1101/gad.307702.117>
- Jackson, S.P., and J. Bartek. 2009. The DNA-damage response in human biology and disease. *Nature*. 461:1071–1078. <https://doi.org/10.1038/nature08467>
- Jette, N., and S.P. Lees-Miller. 2015. The DNA-dependent protein kinase: A multifunctional protein kinase with roles in DNA double strand break repair and mitosis. *Prog. Biophys. Mol. Biol.* 117:194–205. <https://doi.org/10.1016/j.pbiomolbio.2014.12.003>
- Komarova, Y., G. Lansbergen, N. Galjart, F. Grosveld, G.G. Borisy, and A. Akhmanova. 2005. EB1 and EB3 control CLIP dissociation from the ends of growing microtubules. *Mol. Biol. Cell*. 16:5334–5345. <https://doi.org/10.1091/mbc.e05-07-0614>
- Lawrimore, J., T.M. Barry, R.M. Barry, A.C. York, B. Friedman, D.M. Cook, K. Akialis, J. Tyler, P. Vasquez, E. Yeh, and K. Bloom. 2017. Microtubule dynamics drive enhanced chromatin motion and mobilize telomeres in response to DNA damage. *Mol. Biol. Cell*. 28:1701–1711. <https://doi.org/10.1091/mbc.e16-12-0846>
- Li, J., and D.F. Stern. 2005. Regulation of CHK2 by DNA-dependent protein kinase. *J. Biol. Chem.* 280:12041–12050. <https://doi.org/10.1074/jbc.M412445200>
- Li, W., X. Bai, J. Li, Y. Zhao, J. Liu, H. Zhao, L. Liu, M. Ding, Q. Wang, F.Y. Shi, et al. 2019. The nucleoskeleton protein IFFO1 immobilizes broken DNA and suppresses chromosome translocation during tumorigenesis. *Nat. Cell Biol.* 21:1273–1285. <https://doi.org/10.1038/s41556-019-0388-0>
- Lin, Y.F., H.Y. Shih, Z. Shang, S. Matsunaga, and B.P. Chen. 2014. DNA-PKcs is required to maintain stability of Chk1 and Claspin for optimal replication stress response. *Nucleic Acids Res.* 42:4463–4473. <https://doi.org/10.1093/nar/gku116>
- Löblich, M., and P. Jeggo. 2017. A Process of Resection-Dependent Nonhomologous End Joining Involving the Goddess Artemis. *Trends Biochem. Sci.* 42:690–701. <https://doi.org/10.1016/j.tibs.2017.06.011>
- Löffler, H., T. Bochtler, B. Fritz, B. Tews, A.D. Ho, J. Lukas, J. Bartek, and A. Krämer. 2007. DNA damage-induced accumulation of centrosomal Chk1 contributes to its checkpoint function. *Cell Cycle*. 6:2541–2548. <https://doi.org/10.4161/cc.6.20.4810>
- Löffler, H., A. Fechter, F.Y. Liu, S. Poppelreuther, and A. Krämer. 2013. DNA damage-induced centrosome amplification occurs via excessive formation of centriolar satellites. *Oncogene*. 32:2963–2972. <https://doi.org/10.1038/onc.2012.310>
- Lotterberger, F., R.A. Karssemeijer, N. Dimitrova, and T. de Lange. 2015. 53BP1 and the LINC Complex Promote Microtubule-Dependent DSB Mobility and DNA Repair. *Cell*. 163:880–893. <https://doi.org/10.1016/j.cell.2015.09.057>
- Lukas, J., and C. Lukas. 2013. Molecular biology. Shielding broken DNA for a quick fix. *Science*. 339:652–653. <https://doi.org/10.1126/science.1234602>
- Mangeol, P., B. Prevo, and E.J. Peterman. 2016. KymographClear and KymographDirect: two tools for the automated quantitative analysis of molecular and cellular dynamics using kymographs. *Mol. Biol. Cell*. 27:1948–1957. <https://doi.org/10.1091/mbc.e15-06-0404>
- Manning, J.A., and S. Kumar. 2010. A potential role for NEDD1 and the centrosome in senescence of mouse embryonic fibroblasts. *Cell Death Dis.* 1:e35. <https://doi.org/10.1038/cddis.2010.12>
- Mirman, Z., F. Lotterberger, H. Takai, T. Kibe, Y. Gong, K. Takai, A. Bianchi, M. Zimmermann, D. Durocher, and T. de Lange. 2018. 53BP1-RIF1-shieldin counteracts DSB resection through CST- and Pol $\alpha$ -dependent fill-in. *Nature*. 560:112–116. <https://doi.org/10.1038/s41586-018-0324-7>
- Moritz, M., M.B. Braumfeld, V. Guénebaud, J. Heuser, and D.A. Agard. 2000. Structure of the gamma-tubulin ring complex: a template for microtubule nucleation. *Nat. Cell Biol.* 2:365–370. <https://doi.org/10.1038/35014058>
- Mullee, L.L., and C.G. Morrison. 2016. Centrosomes in the DNA damage response—the hub outside the centre. *Chromosome research: an international journal on the molecular, supramolecular and evolutionary aspects of chromosome biology. Chromosome Res.* 24:35–51.
- Nishi, R., Y. Okuda, E. Watanabe, T. Mori, S. Iwai, C. Masutani, K. Sugawara, and F. Hanaoka. 2005. Centrin 2 stimulates nucleotide excision repair by interacting with xeroderma pigmentosum group C protein. *Mol. Cell Biol.* 25:5664–5674. <https://doi.org/10.1128/MCB.25.13.5664-5674.2005>
- Noordermeer, S.M., S. Adam, D. Setiapatra, M. Barazas, S.J. Pettitt, A.K. Ling, M. Olivieri, A. Álvarez-Quilón, N. Moatti, M. Zimmermann, et al. 2018.

- The shieldin complex mediates 53BP1-dependent DNA repair. *Nature*. 560:117–121. <https://doi.org/10.1038/s41586-018-0340-7>
- Ochi, T., A.N. Blackford, J. Coates, S. Jhujh, S. Mehmood, N. Tamura, J. Travers, Q. Wu, V.M. Draviam, C.V. Robinson, et al. 2015. PAXX, a paralog of XRCC4 and XLF, interacts with Ku to promote DNA double-strand break repair. *Science*. 347:185–188. <https://doi.org/10.1126/science.1261971>
- Palazzo, R.E., J.M. Vogel, B.J. Schnackenberg, D.R. Hull, and X. Wu. 2000. Centrosome maturation. *Curr. Top. Dev. Biol.* 49:449–470. [https://doi.org/10.1016/S0070-2153\(99\)49021-0](https://doi.org/10.1016/S0070-2153(99)49021-0)
- Pannunzio, N.R., G. Watanabe, and M.R. Lieber. 2018. Nonhomologous DNA end-joining for repair of DNA double-strand breaks. *J. Biol. Chem.* 293:10512–10523. <https://doi.org/10.1074/jbc.TM117.000374>
- Poruchynsky, M.S., E. Komlodi-Pasztor, S. Trostel, J. Wilkerson, M. Regairaz, Y. Pommier, X. Zhang, T. Kumar Maity, R. Robey, M. Burotto, et al. 2015. Microtubule-targeting agents augment the toxicity of DNA-damaging agents by disrupting intracellular trafficking of DNA repair proteins. *Proc. Natl. Acad. Sci. USA*. 112:1571–1576. <https://doi.org/10.1073/pnas.1416418112>
- Rastogi, R.P., A. Richa, A. Kumar, M.B. Tyagi, and R.P. Sinha. 2010. Molecular mechanisms of ultraviolet radiation-induced DNA damage and repair. *J. Nucleic Acids*. 2010:592980. <https://doi.org/10.4061/2010/592980>
- Riballo, E., M. Kühne, N. Rief, A. Doherty, G.C. Smith, M.J. Recio, C. Reis, K. Dahm, A. Fricke, A. Krempler, et al. 2004. A pathway of double-strand break rejoining dependent upon ATM, Artemis, and proteins locating to gamma-H2AX foci. *Mol. Cell*. 16:715–724. <https://doi.org/10.1016/j.molcel.2004.10.029>
- Robles, S.J., and G.R. Adami. 1998. Agents that cause DNA double strand breaks lead to p16INK4a enrichment and the premature senescence of normal fibroblasts. *Oncogene*. 16:1113–1123. <https://doi.org/10.1038/sj.onc.1201862>
- Ross, J.L., M.Y. Ali, and D.M. Warshaw. 2008. Cargo transport: molecular motors navigate a complex cytoskeleton. *Curr. Opin. Cell Biol.* 20:41–47. <https://doi.org/10.1016/j.ceb.2007.11.006>
- Roukos, V., T.C. Voss, C.K. Schmidt, S. Lee, D. Wangsa, and T. Misteli. 2013. Spatial dynamics of chromosome translocations in living cells. *Science*. 341:660–664. <https://doi.org/10.1126/science.1237150>
- Saji, M., V. Vasko, F. Kada, E.H. Allbritton, K.D. Burman, and M.D. Ringel. 2005. Akt1 contains a functional leucine-rich nuclear export sequence. *Biochem. Biophys. Res. Commun.* 332:167–173. <https://doi.org/10.1016/j.bbrc.2005.04.109>
- Schrank, B.R., T. Aparicio, Y. Li, W. Chang, B.T. Chait, G.G. Gundersen, M.E. Gottesman, and J. Gautier. 2018. Nuclear ARP2/3 drives DNA break clustering for homology-directed repair. *Nature*. 559:61–66. <https://doi.org/10.1038/s41586-018-0237-5>
- Shang, Z.F., B. Huang, Q.Z. Xu, S.M. Zhang, R. Fan, X.D. Liu, Y. Wang, and P.K. Zhou. 2010. Inactivation of DNA-dependent protein kinase leads to spindle disruption and mitotic catastrophe with attenuated checkpoint protein 2 Phosphorylation in response to DNA damage. *Cancer Res.* 70:3657–3666. <https://doi.org/10.1158/0008-5472.CAN-09-3362>
- Sugihara, E., M. Kanai, S. Saito, T. Nitta, H. Toyoshima, K. Nakayama, K.I. Nakayama, K. Fukasawa, M. Schwab, H. Saya, and M. Miwa. 2006. Suppression of centrosome amplification after DNA damage depends on p27 accumulation. *Cancer Res.* 66:4020–4029. <https://doi.org/10.1158/0008-5472.CAN-05-3250>
- Suizu, F., N. Hirata, K. Kimura, T. Edamura, T. Tanaka, S. Ishigaki, T. Donia, H. Noguchi, T. Iwanaga, and M. Noguchi. 2016. Phosphorylation-dependent Akt-Inversin interaction at the basal body of primary cilia. *EMBO J.* 35:1346–1363. <https://doi.org/10.15252/embj.201593003>
- Tomida, J., K.I. Takata, S. Bhetawal, M.D. Person, H.P. Chao, D.G. Tang, and R.D. Wood. 2018. FAM35A associates with REV7 and modulates DNA damage responses of normal and BRCA1-defective cells. *EMBO J.* 37:37. <https://doi.org/10.15252/embj.201899543>
- Vertii, A., M. Ivshina, W. Zimmerman, H. Hehnly, S. Kant, and S. Doxsey. 2016. The Centrosome Undergoes Plk1-Independent Interphase Maturation during Inflammation and Mediates Cytokine Release. *Dev. Cell*. 37:377–386. <https://doi.org/10.1016/j.devcel.2016.04.023>
- Wakefield, J.G., D.J. Stephens, and J.M. Tavaré. 2003. A role for glycogen synthase kinase-3 in mitotic spindle dynamics and chromosome alignment. *J. Cell Sci.* 116:637–646. <https://doi.org/10.1242/jcs.00273>
- Wang, C.Y., Y.H. Kao, P.Y. Lai, W.Y. Chen, and B.C. Chung. 2013. Steroidogenic factor 1 (NR5A1) maintains centrosome homeostasis in steroidogenic cells by restricting centrosomal DNA-dependent protein kinase activation. *Mol. Cell Biol.* 33:476–484. <https://doi.org/10.1128/MCB.01064-12>
- Wang, C.Y., E.Y. Huang, S.C. Huang, and B.C. Chung. 2015. DNA-PK/Chk2 induces centrosome amplification during prolonged replication stress. *Oncogene*. 34:1263–1269. <https://doi.org/10.1038/ncr.2014.74>
- Woodruff, J.B., O. Wueseke, and A.A. Hyman. 2014. Pericentriolar material structure and dynamics. *Philos. Trans. R. Soc. Lond. B Biol. Sci.* 369:20130459. <https://doi.org/10.1098/rstb.2013.0459>
- Xu, G., J.R. Chapman, I. Brandsma, J. Yuan, M. Mistrik, P. Bouwman, J. Bartkova, E. Gogola, D. Warmerdam, M. Barazas, et al. 2015. REV7 counteracts DNA double-strand break resection and affects PARP inhibition. *Nature*. 521:541–544. <https://doi.org/10.1038/nature14328>
- Zgheib, O., K. Pataky, J. Brugger, and T.D. Halazonetis. 2009. An oligomerized 53BP1 tudor domain suffices for recognition of DNA double-strand breaks. *Mol. Cell Biol.* 29:1050–1058. <https://doi.org/10.1128/MCB.01011-08>
- Zhang, X., Q. Chen, J. Feng, J. Hou, F. Yang, J. Liu, Q. Jiang, and C. Zhang. 2009. Sequential phosphorylation of Nedd1 by Cdk1 and Plk1 is required for targeting of the gammaTuRC to the centrosome. *J. Cell Sci.* 122:2240–2251. <https://doi.org/10.1242/jcs.042747>
- Zhao, J., Y. Zou, H. Liu, H. Wang, H. Zhang, W. Hou, X. Li, X. Jia, J. Zhang, L. Hou, and B. Zhang. 2014. TEIF associated centrosome activity is regulated by EGF/PI3K/Akt signaling. *Biochim. Biophys. Acta.* 1843:1851–1864. <https://doi.org/10.1016/j.bbamcr.2014.04.021>
- Zheng, Y., M.L. Wong, B. Alberts, and T. Mitchison. 1995. Nucleation of microtubule assembly by a gamma-tubulin-containing ring complex. *Nature*. 378:578–583. <https://doi.org/10.1038/378578a0>
- Zimmermann, M., F. Lotterberger, S.B. Buonomo, A. Sfeir, and T. de Lange. 2013. 53BP1 regulates DSB repair using Rif1 to control 5' end resection. *Science*. 339:700–704. <https://doi.org/10.1126/science.1231573>

## Supplemental material

A Related to Figure 1A,B

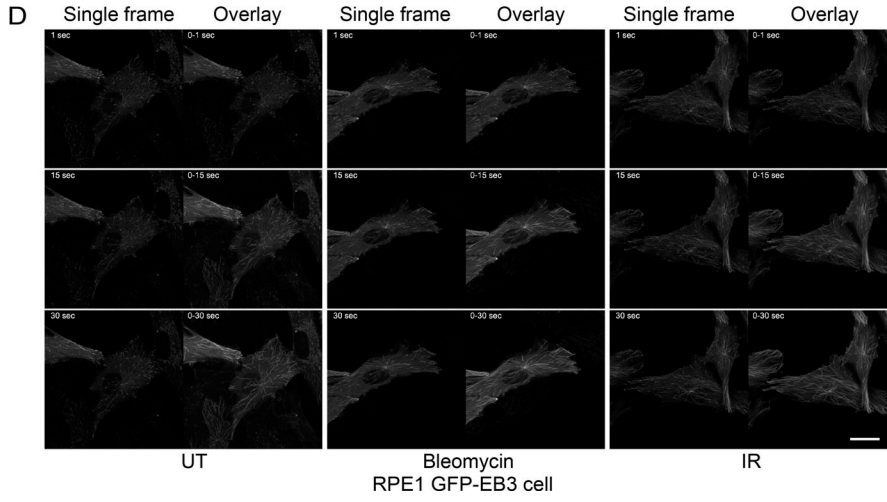
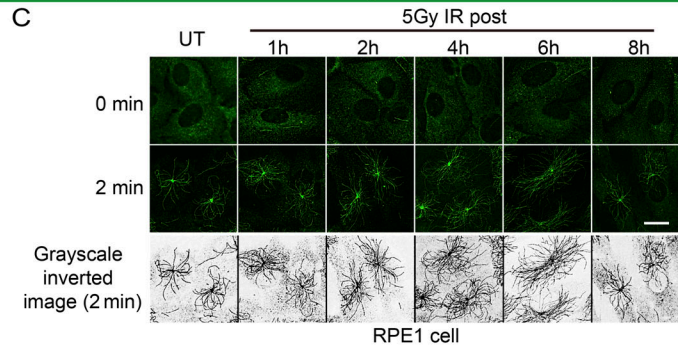
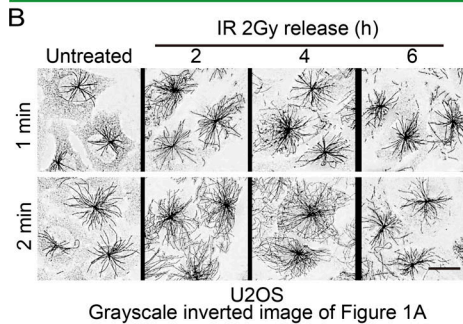
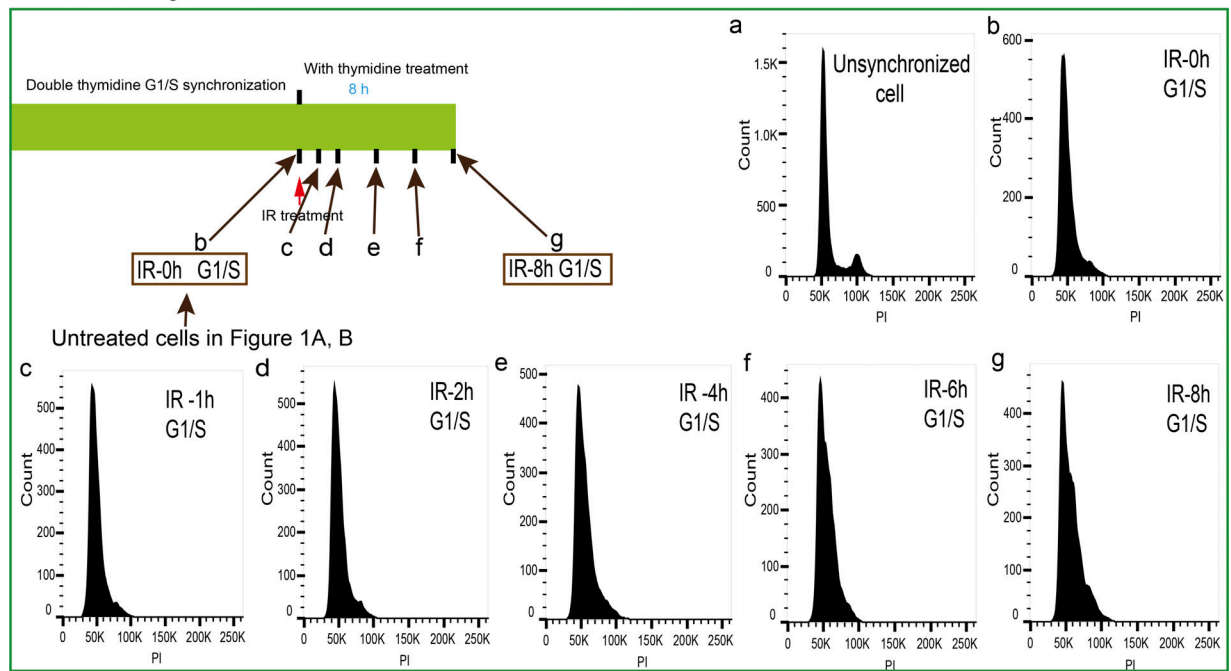
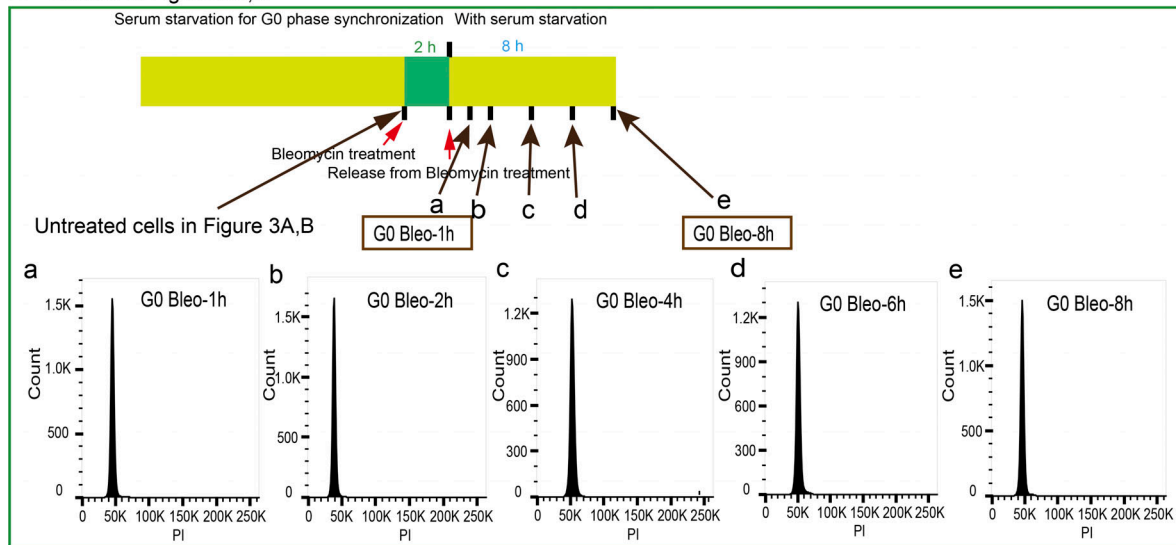
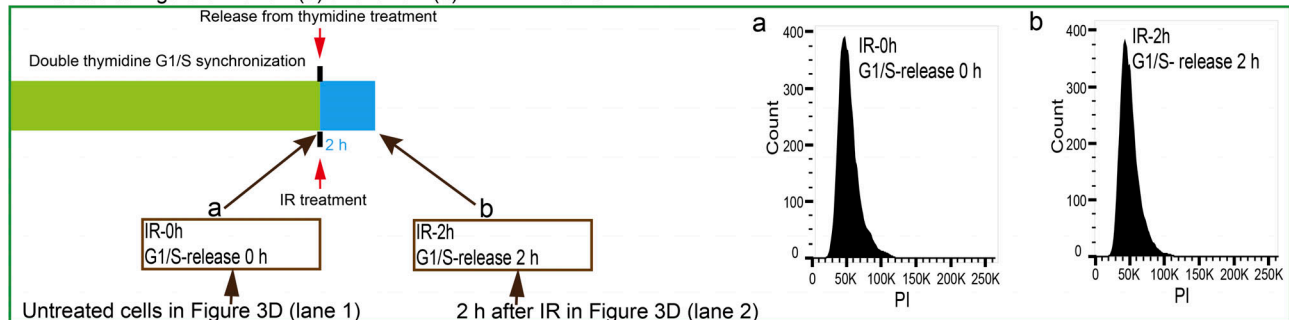


Figure S1. **DSBs lead to DMSR.** (A) The experiment procedure for DMSR analysis in G1 cells is shown. The phase of U2OS cell cycle in indicated time points was determined by flow cytometry. (B) Grayscale inverted images of Fig. 1A show the increased microtubule number originated from the centrosomes in IR-treated cells. (C) RPE-1 cells were synchronized at G1/S phase, treated with 5 Gy IR, released, and fixed at indicated time points. DMSR was determined by microtubule regrowth assay. Upper: Microtubules (green) were stained with anti- $\beta$ -tubulin antibody. Scale bar, 20  $\mu$ m. Lower: Grayscale inverted images show the increased microtubule number originated from the centrosome in IR-treated cells compared with untreated cells. (D) DMSR is confirmed by live-imaging time-lapse experiments. Overlaid GFP-EB3 signal indicated the newly synthesized microtubule tracks within indicated time periods (overlay). The single frames of GFP-EB3 comet associated with the growing microtubule plus ends in steady status (single frame) are also displayed. Images of projections at indicated time points and spanning 0–1 s, 0–15 s, and 0–30 s are shown. See also Videos 1, 2, and 3. Scale bar, 20  $\mu$ m. UT, untreated; sec, seconds; PI, propidium iodide.

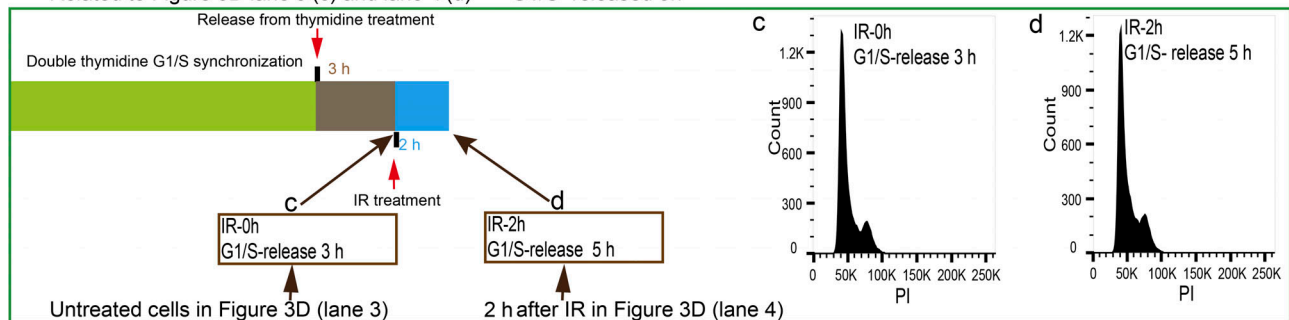
A Related to Figure 3 A,B



B Related to Figure 3D lane 1 (a) and lane 2 (b)



Related to Figure 3D lane 3 (c) and lane 4 (d) G1/S- released 3h



Related to Figure 3D lane 5 (e) and lane 6 (f) G1/S- released 5h

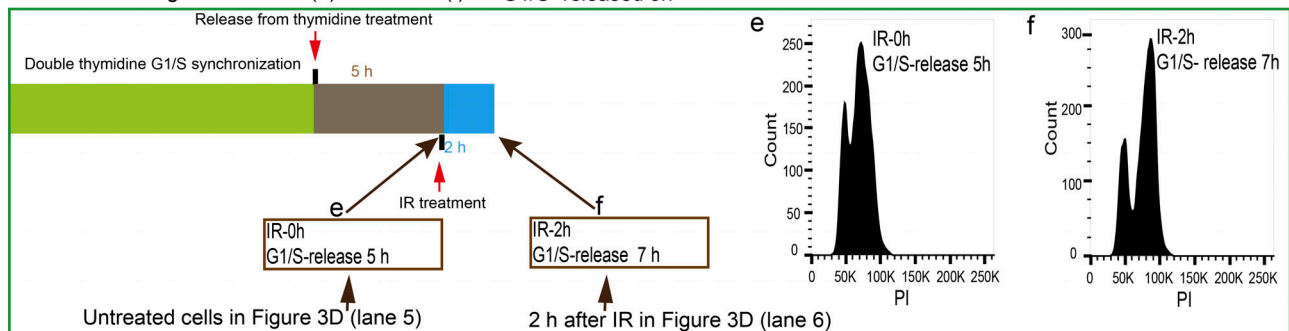


Figure S2. **DMSR only occurs in G0 or G1 cells.** (A) The experimental procedure for DMSR analysis in serum-starved G0 cells is shown. The U2OS cell cycle stage in indicated time points was determined by flow cytometry (related to Fig. 3, A and B). (B) U2OS cells were synchronized at G1/S and released for indicated time points. Cells were then treated with 2 Gy IR, and DMSR was determined at 2 h after IR treatment by microtubule regrowth assay. The detailed procedures and U2OS cell cycle stage at each time points are shown. Cell cycle stage was determined by flow cytometry. Upper: G1/S phase cell. Middle: G1/S released 3 h. Lower: G1/S-released 5 h. PI, propidium iodide.

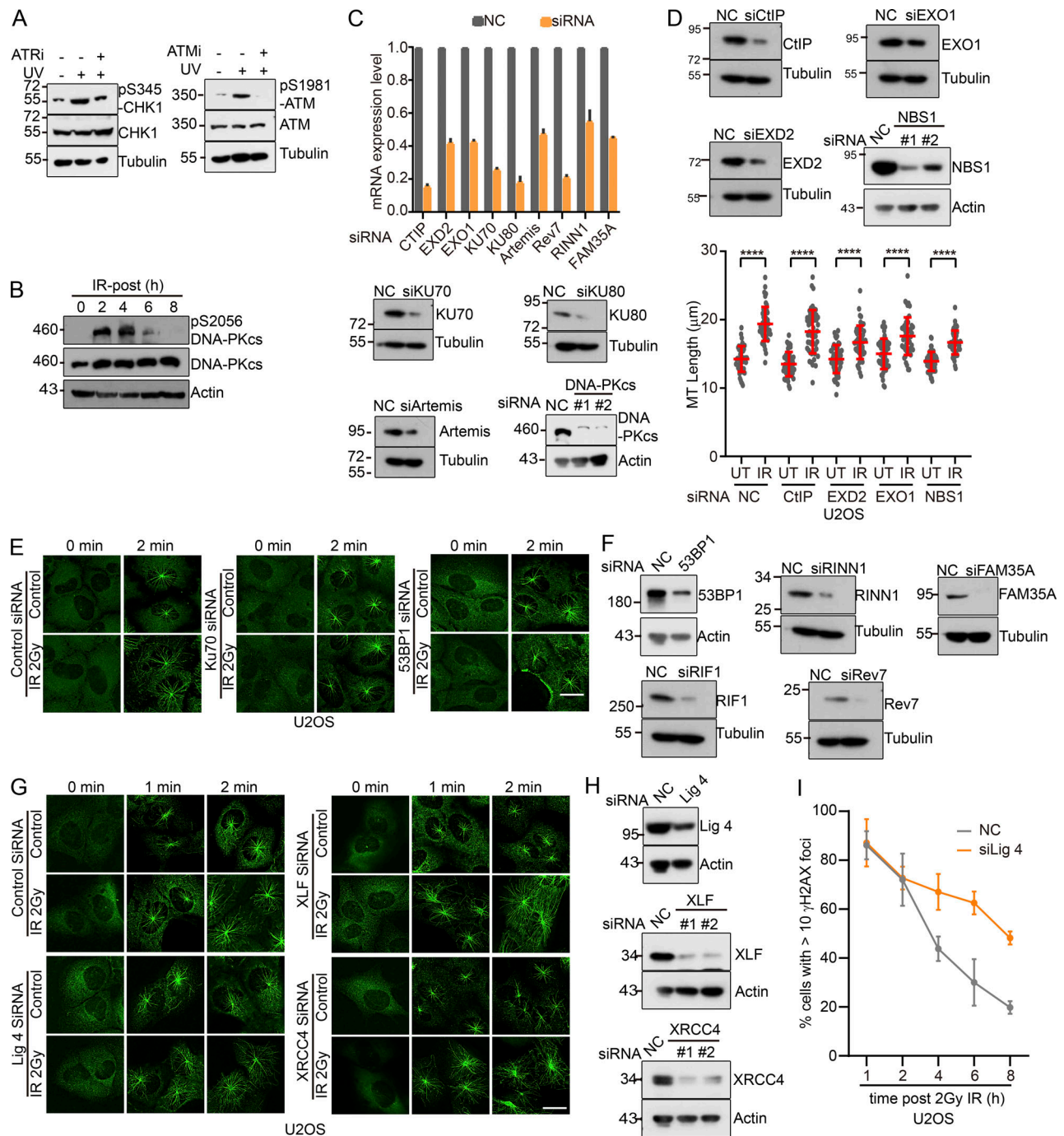


Figure S3. **c-NHEJ is required for DMSR.** (A) The efficiency of ATR inhibitor or ATM inhibitor was confirmed by probing with pS345-CHK1 antibody or pS1981-ATM antibody, respectively. (B) The time course of DNA-PK activation after RPE-1 cells were exposed to 5 Gy IR in G1/S. DNA-PK activation was determined by immunoblotting with anti-pS2056 DNA-PKcs antibody. (C) Left: Quantitative RT-PCR shows the knockdown efficiency of indicated genes. Right: Western blot analysis shows the efficiency of indicated siRNAs. RPE-1 cells were transfected with indicated siRNAs. Cells were then collected and extracted after 48 h of transfections. The efficiency was measured by indicated antibodies. (D) Depletion of CtIP or other proteins responsible for end resection, such as EXD2, EXO1, and NBS1, at G1 phase does not affect DMSR. U2OS cells were transfected with indicated siRNAs and synchronized at G1/S phase. Cells were then exposed to 2 Gy IR and recovered for 4 h. Left: Western blot analysis shows the efficiency of indicated siRNAs. Right: Microtubule nucleation ability was determined by microtubule regrowth assay. Quantitation of microtubule length was assayed as in Fig. 1. This experiment and the experiment in Fig. 4 B belong to a same group of experiments. Thus, the same data for the control group was included in this figure and Fig. 4 B. (E) DMSR is significantly inhibited by depletion of 53BP1 or Ku70. U2OS cells were transfected with indicated siRNA and synchronized at G1/S phase. Cells then were exposed to 2 Gy IR and recovered for 4 h. Microtubules were stained with anti- $\beta$ -tubulin antibody. Scale bar, 20  $\mu$ m. (F) Western blot analysis shows the efficiency of indicated siRNAs. (G) Depletion of Ligase 4, XRCC4, or XLF, which are required for c-NHEJ, promote DMSR in U2OS cells. Microtubules (green) were stained with anti- $\beta$ -tubulin antibody. Scale bar, 20  $\mu$ m. (H) Western blot analysis shows the efficiency of indicated siRNAs. (I) The activation of DDR and kinetics of DNA damage repair in IR-treated U2OS control cells or siLig4 cells was determined by  $\gamma$ H2AX foci formation ( $n > 100$ ). \*\*\*\*,  $P < 0.0001$ ; MT, microtubule; UT, untreated.



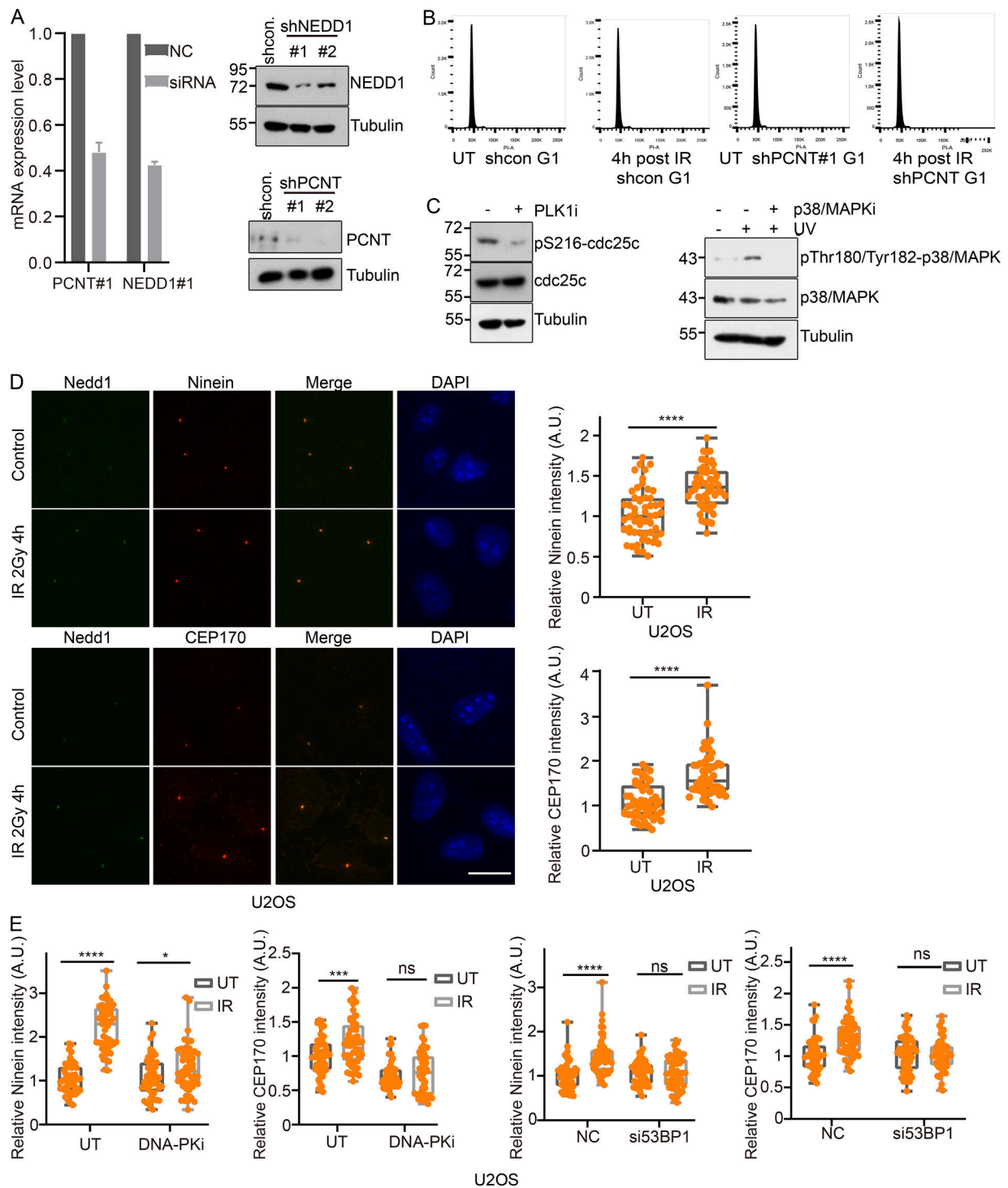
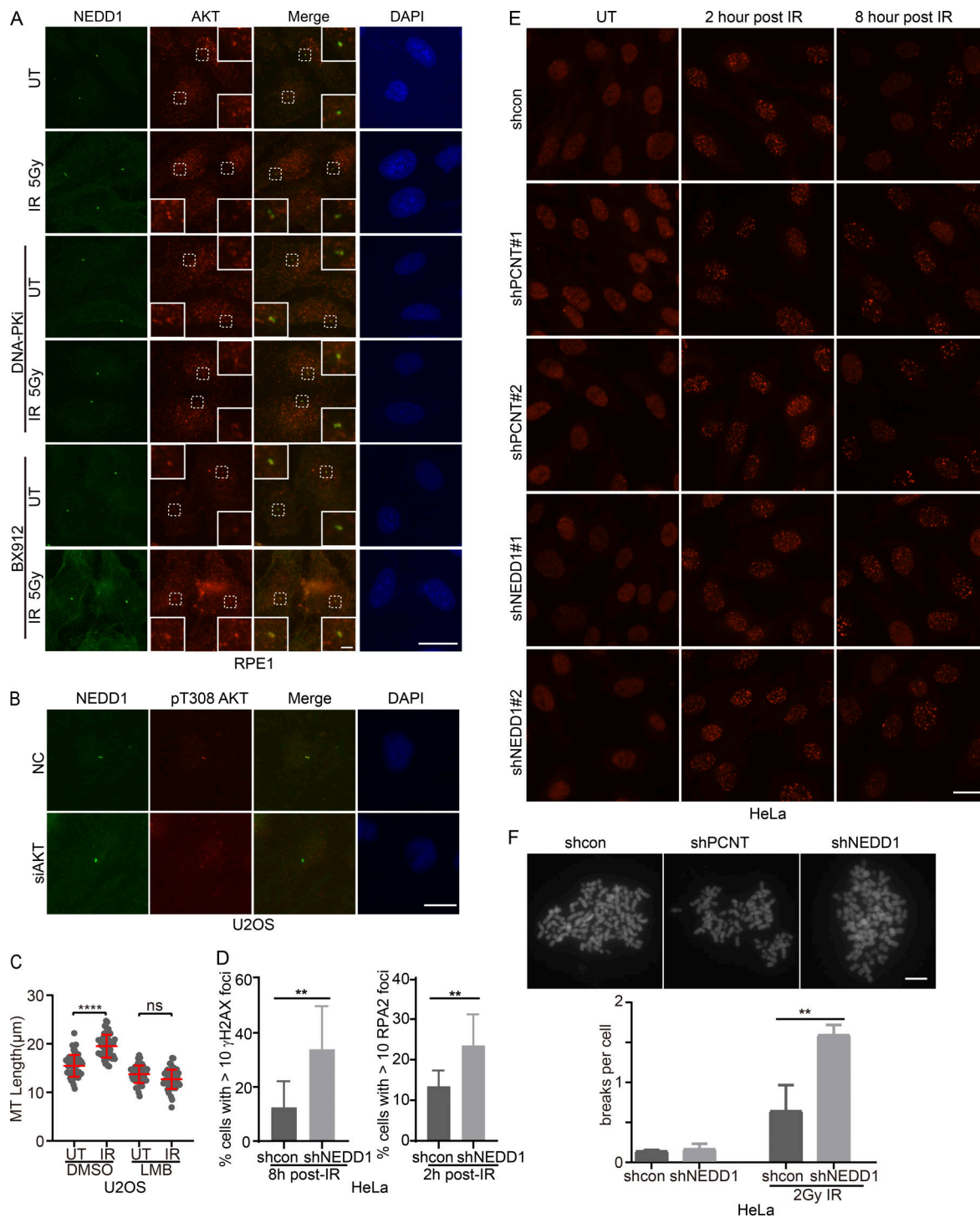


Figure S4. **DMSR depends on interphase centrosome maturation.** (A) Quantitative RT-PCR and Western blot analysis show the siRNA efficiency of centrosome proteins NEDD1 and PCNT in U2OS cells. (B) Cell cycle stage was determined by flow cytometry in shcon or shPCNT U2OS cells (related to Fig. 5 B). Both shcon and shPCNT cells remained in G1 phase after IR treatment. (C) The efficiency of PLK1 inhibitor or p38 inhibitor was confirmed by pS216-CDC25C antibody or pThr180/Tyr182-p38 antibody. (D) Centrosome subdistal appendage protein Ninein and CEP170 obviously increased at the centrosomes after cells were exposed to IR in U2OS cells. Left: Immunofluorescence showed DSB-induced accumulation of Ninein or CEP170 in cells treated with 2 Gy IR. Right: Semiquantitative analysis of the relative signal intensity of subdistal appendage proteins at the centrosomes from control or IR-treated cells is shown. Scale bar, 20  $\mu$ m. (E) Subdistal appendage protein recruitment at the centrosomes depends on DNA-PK kinase activity in U2OS cells. Right: DNA-PK inhibitor inhibited the IR-induced accumulation of Ninein and CEP170 at the centrosomes. Semiquantitative analysis of Ninein and CEP170 signal intensity at the centrosomes from control or DNA-PK inhibitor treated cells is shown. Left: IR-induced recruitment of Ninein and CEP170 at centrosomes requires 53BP1. Semiquantitative analysis of Ninein and CEP170 signal intensity at the centrosomes from control or 53BP1-depleted cells is shown in box plot ( $n > 50$ ). \*\*\*\*,  $P < 0.0001$ ; \*\*\*,  $P < 0.001$ ; \*,  $P < 0.05$ ; ns, not significant. A.U., arbitrary units; UT, untreated; PI, propidium iodide.



**Figure S5. DNA-PK activates AKT at the centrosomes.** (A) AKT colocalized with centrosomal protein NEDD1. RPE-1 cells were coimmunostained with NEDD1 and AKT after different treatments. Colocalization of NEDD1 and AKT is shown in the Merge panel. Scale bar, 20 μm for labeled panel, 2 μm for magnified images. (B) pT308 AKT colocalized with centrosomal protein NEDD1. Depletion of AKT by siRNA abolished pT308 AKT on the centrosomes, indicating the specificity of anti-pT308 AKT antibody. Scale bar, 20 μm. (C) U2OS cells were treated with 2 Gy IR at 2 h after 200 nM leptomycin B pretreatment. The rate of microtubule polymerization was determined by microtubule regrowth assay at 2 h after IR treatment. Quantitation of microtubule length after IR treatment showed the rate of microtubule polymerization ( $n > 50$ ). (D) NEDD1 depletion affected the NHEJ repair process and led to increased end resection of DSBs. The efficiency of NHEJ was indicated by γH2AX foci 8 h after IR treatment. The end resection was measured by RPA2 foci formation 2 h after IR treatment in HeLa cells. Quantitative results are shown ( $n > 50$ ). (E) Representative images show the 53BP1 foci formation in shcon, shPCNT, or shNEDD1 cells after 5 Gy IR treatment in HeLa cells at indicated time points. Scale bar, 20 μm. (F) Upper: Representative images show chromosome breaks in shcon, shPCNT, or shNEDD1 HeLa cells without IR treatment. Chromosome DNA is stained with Hoechst, and there were no chromosome breaks in shPCNT or shNEDD1 cells without IR treatment. Lower: Quantitation of chromosome breaks per cell in shcon or shNEDD1 cells with or without IR treatment ( $n > 30$ ). \*\*\*\*,  $P < 0.0001$ ; \*\*,  $P < 0.01$ ; ns, not significant. MT, microtubule; UT, untreated.

**Video 1. GFP-EB3 movement in untreated RPE1 cells.** Related to [Fig. 2 A](#) and [Fig. S1 D](#) (untreated [UT]). Microtubule polymerization was determined by live-imaging time-lapse experiments in RPE-1 cells stably expressing GFP-EB3. GFP-EB3 comets associated with the growing microtubule plus end in steady status are shown (left), and overlaid GFP-EB3 signal shows the newly synthesized microtubule tracks within indicated time period (right). The time-lapse images were gathered for 30 s at 1-s intervals using Airyscan and time series of Zeiss confocal microscope in the UT control G1 RPE-1 cells. The video of the single images and overlaid images was made by Adobe Premiere, the video duration was 5 s, and the frame rate was 6 frames per second.

**Video 2. GFP-EB3 movement in bleomycin-treated RPE1 cells.** Related to [Fig. 2 A](#) and [Fig. S1 D](#) (bleomycin). DMSR was confirmed by live-imaging time-lapse experiments in RPE-1 cells stably expressing GFP-EB3. GFP-EB3 comets associated with the growing microtubule plus end in steady status (left) are shown, and overlaid GFP-EB3 signal shows the newly synthesized microtubule tracks within indicated time period (right). G1 RPE-1 cells were treated with bleomycin (5 µg/ml) for 2 h. At 4 h after bleomycin treatment, images were gathered for 30 s at 1-s intervals using Airyscan and time series of Zeiss confocal microscope. The video of the single image and overlaid images was made by Adobe Premiere, the video duration was 5 s, and the frame rate was 6 frames per second.

**Video 3. GFP-EB3 movement in IR-treated RPE1 cells.** Related to [Fig. 2 A](#) and [Fig. S1 D](#) (IR). DMSR was confirmed by live-imaging time-lapse experiments in RPE-1 cells stably expressing GFP-EB3. GFP-EB3 comets associated with the growing microtubule plus end in steady status are shown (left), and overlaid GFP-EB3 signal shows the newly synthesized microtubule tracks within indicated time period (right). G1 RPE-1 cells were treated with IR (5 Gy). At 4 h after IR treatment, images were gathered for 30 s at 1-s intervals using Airyscan and time series of Zeiss confocal microscope. The video of the single image and overlaid images was made by Adobe Premiere, the video duration was 5 s, and the frame rate was 6 frames per second.

**Video 4. GFP-EB3 movement in untreated RPE1 cells.** Related to [Fig. 2 C](#) (untreated). DMSR-related microtubule nucleation capacity was analyzed by live-imaging time-lapse experiments in RPE-1 cells stably expressing GFP-EB3. GFP-EB3 comets associated with the growing microtubule plus ends in untreated control cells are shown. RPE-1 cells stably expressing GFP-EB3 were synchronized in G1 phase. Images were gathered for 30 s at 1-s intervals using Airyscan and time series of Zeiss confocal microscope in untreated G1 RPE-1 cells. The video was made using these images in chronologic order by Adobe Premiere, the video duration was 5 s, and the frame rate was 6 frames per second.

**Video 5. GFP-EB3 movement in RPE-1 cells at 1 h after IR treatment.** Related to [Fig. 2 C](#) (1 h after IR). DMSR-related microtubule nucleation capacity under IR treatment was analyzed by live-imaging time-lapse experiments in RPE-1 cells stably expressing GFP-EB3. GFP-EB3 comets associated with the growing microtubule plus ends at 1 h after IR are shown. G1 RPE-1 cells were treated with IR (5 Gy). At 1 h after IR treatment, images were gathered for 30 s at 1-s intervals using Airyscan and time series of Zeiss confocal microscope. The video was made using these images in chronologic order by Adobe Premiere, the video duration was 5 s, and the frame rate was 6 frames per second.

**Video 6. GFP-EB3 movement in RPE1 cells at 2 h after IR treatment.** Related to [Fig. 2 C](#) (2 h after IR). DMSR-related microtubule nucleation capacity under IR treatment was analyzed by live-imaging time-lapse experiments in RPE-1 cells stably expressing GFP-EB3. GFP-EB3 comets associated with the growing microtubule plus ends at 2 h after IR are shown. G1 RPE-1 cells were treated with IR (5 Gy). At 2 h after IR treatment, images were gathered for 30 s at 1-s intervals using Airyscan and time series of Zeiss confocal microscope. The video was made using these images in chronologic order by Adobe Premiere, the video duration was 5 s, and the frame rate was 6 frames per second.

**Video 7. GFP-EB3 movement in RPE1 cells at 4 h after IR treatment.** Related to [Fig. 2 C](#) (4 h after IR). DMSR-related microtubule nucleation capacity under IR treatment was analyzed by live-imaging time-lapse experiments in RPE-1 cells stably expressing GFP-EB3. GFP-EB3 comets associated with the growing microtubule plus ends at 4 h after IR are shown. G1 RPE-1 cells were treated with IR (5 Gy). At 4 h after IR treatment, images were gathered for 30 s at 1-s intervals using Airyscan and time series of Zeiss confocal microscope. The video was made using these images in chronologic order by Adobe Premiere, the video duration was 5 s, and the frame rate was 6 frames per second.

**Video 8. GFP-EB3 movement in untreated RPE1 cells.** Related to [Fig. 2 E](#) (untreated). Microtubule nucleation capacity was analyzed by live-imaging time-lapse experiments in RPE-1 cells stably expressing GFP-EB3. GFP-EB3 comets associated with the growing microtubule plus ends in untreated control cells are shown. RPE-1 cells were synchronized in G1/S phase. Images were gathered for 30 s at 1-s intervals using Airyscan and time series of Zeiss confocal microscope in untreated G1 RPE-1 cells. The video was made using these images in chronologic order by Adobe Premiere, the video duration was 5 s, and the frame rate was 6 frames per second.

Video 9. **GFP-EB3 movement in RPE1 cells at 4 h after bleomycin treatment.** Related to Fig. 2 E (bleomycin after 4 h). Microtubule nucleation capacity after bleomycin treatment was analyzed by live-imaging time-lapse experiments in RPE-1 cells stably expressing GFP-EB3. GFP-EB3 comets associated with the growing microtubule plus ends at 4 h after bleomycin treatment are shown. G1 RPE-1 cells were treated with bleomycin (5  $\mu\text{g}/\text{ml}$ ) for 2 h. At 4 h after bleomycin treatment, images were gathered for 30 s at 1-s intervals using Airyscan and time series of Zeiss confocal microscope. The video was made using these images in chronologic order by Adobe Premiere, the video duration was 5 s, and the frame rate was 6 frames per second.

Video 10. **DSB mobility in shcon-treated HeLa cells.** Related to Fig. 9 A (shcon). DSB mobility was analyzed by live-imaging time-lapse experiments in HeLa cells expressing GFP-53BP1 TD domain (residues 1220–1711). DSB mobility was shown through GFP-53BP1 TD foci. Scrambled shRNA-treated G1 HeLa cells were treated with 2 Gy IR. At 1 h after IR treatment, images were gathered for 10 min at 30-s intervals using Z-stacks function by Olympus microscope. Z-stacks images at each time point were first handled by deconvolution using Olympus cellSens dimension software. These images were then used to make a video that lasts 10 s at a frame rate of 2 frames per second by Adobe Premiere. Scale bar, 10  $\mu\text{M}$ .

Video 11. **DSB mobility in shPCNT-treated HeLa cells.** Related to Fig. 9 A (shPCNT). DSB mobility was analyzed by live-imaging time-lapse experiments in HeLa cells expressing GFP-53BP1 TD domain (residues 1220–1711). DSB mobility was shown through GFP-53BP1 TD foci. shPCNT-treated G1 HeLa cells were treated with 2 Gy IR. At 1 h after IR treatment, images were gathered for 10 min at 30-s intervals using Z-stacks function by Olympus microscope. Z-stacks images at each time point was first handled by deconvolution using Olympus cellSens dimension software. These images were then used to make a video that lasts 10 s at a frame rate of 2 frames per second by Adobe Premiere. Scale bar, 10  $\mu\text{M}$ .

**Table S1 is provided online as a separate Word file and lists reagents, siRNA or shRNA sequences, and quantitative PCR primers used in this study.**